
This is an electronic reprint of the original article.
This reprint may differ from the original in pagination and typographic detail.

Gholami Haghighi Fard, Morteza; Hostikka, Simo

Unraveling the surface heat flux heterogeneity in cone calorimetry of cylindrical charring material : Insights from experiments and 2D modeling

Published in:
Fire Safety Journal

DOI:
[10.1016/j.firesaf.2024.104119](https://doi.org/10.1016/j.firesaf.2024.104119)

Published: 01/05/2024

Document Version
Publisher's PDF, also known as Version of record

Published under the following license:
CC BY

Please cite the original version:
Gholami Haghighi Fard, M., & Hostikka, S. (2024). Unraveling the surface heat flux heterogeneity in cone calorimetry of cylindrical charring material : Insights from experiments and 2D modeling. *Fire Safety Journal*, 145, Article 104119. <https://doi.org/10.1016/j.firesaf.2024.104119>



Unraveling the surface heat flux heterogeneity in cone calorimetry of cylindrical charring material: Insights from experiments and 2D modeling

Morteza Gholami Haghighi Fard, Simo Hostikka *

Department of Civil Engineering, Aalto University, Rakentajanaukio 4 A, Espoo, 02150, Finland

ARTICLE INFO

Keywords:

Charring polymer
Cone calorimeter
FDS
Cylindrical fuel
Radiative flux
Convective flux

ABSTRACT

Although originally designed for planar samples, cone calorimeter is frequently used for the flammability assessment and pyrolysis modeling of non-planar objects, like electrical cables. Prescribing the boundary conditions for the numerical models of such objects requires knowledge about the radiative and convective heat fluxes along the sample circumference. In this work, we performed gasification and flaming experiments and 2D numerical simulations on birch cylinders. During the gasification of a single-rod, the char front propagated faster vertically than horizontally, while similar rates were observed in the flaming condition. With five rods, U- and n-shaped char fronts were observed in gasification and flaming conditions, respectively. From the simulations, we extracted detailed heat flux distributions, with main deviation from flat samples being the steep reduction in incident radiation between the top and sides of the cylinders. Moreover, in five-rod configurations, radiative flux to the sides of the central rod increases up to 10 (gasification) and 20 kW m⁻² (flaming). On the outermost rod, the descending flame induces downward-moving waves of heat fluxes with amplitudes 20 kW m⁻² for convection and 15 kW m⁻² for radiation. Simplified expressions for the heat transfer boundary conditions were tabulated for practical engineering applications.

1. Introduction

In fire safety studies, the performance of materials is often evaluated by means of bench-scale measurements, where a small specimen is analyzed under a carefully controlled fire test environment. In these methods, the sample is exposed to a well-defined radiative source, and the measurements are performed under either aerobic or anaerobic conditions. Such tests are applied to record the rate of mass loss and energy release of the sample while being decomposed, thus providing necessary information to experimentally assess the fire performance of the specimen. Examples of such instruments are Fire Propagation Apparatus-FPA-(ASTM E2058 [1]), Controlled Atmosphere Pyrolysis Apparatus-CAPA- [2,3], and most commonly used, Cone Calorimeter (ISO 5660 [4]). These instruments were originally designed to measure the fire performance of planar slabs of construction materials, where flat samples are cut from large sheets of the products. Nevertheless, polymeric materials in a cylindrical shape are the primary fuel sources in numerous household, industrial, and wildland fires. Thermoplastic polymers used as the coverings of electrical cables and dead vegetation are examples of such cylindrical fuel sources. Electrical wires and cables form 5% of the first ignited materials in home structure fires [5]. In nuclear power plants, cable insulation ranks as the second most frequently ignited component, after oil [6]. Twigs, shrubs, dead tree

trunks, and pine needles are the primary cylindrical fuels in wildland surface fires [7]. Although standard tests are commonly performed on these non-planar materials, the implications of the non-planar geometry on the applicability of the test data in large-scale fire scenarios have not been comprehensively studied. Yet, the measurement data from standard tests are necessary for the calibration and validation of numerical methods developed for material pyrolysis modeling.

Over the past few decades, numerous attempts have been made to develop numerical models for simulating cables in the cone calorimeter, including works by Hostikka and Matala [8,9], Matala [10], and Hehnen et al. [11]. However, these models relied on a series of simplifying assumptions. For instance, they mapped the cylindrical geometry of cables, which consists of jacket, insulation, and conductor layers, onto a rectangular surrogate volume with corresponding layers of materials. Moreover, the radiative exposure of the conical heater on the cylindrical cable surface was modeled as a virtual external flux on the flat surfaces of the surrogate rectangle. Such models fail to capture the physical phenomena that arise from the curvature of the samples. Specifically, the radiative and convective flux distributions over the cylindrical bodies differ significantly from those over flat plates [12]. These simplifications typically lead to significant uncertainties, requiring the modeler to introduce additional compensation factors and parameters to mitigate the possible inaccuracies.

* Corresponding author.

E-mail address: simo.hostikka@aalto.fi (S. Hostikka).

<https://doi.org/10.1016/j.firesaf.2024.104119>

Received 13 November 2023; Received in revised form 24 January 2024; Accepted 13 February 2024

Available online 14 February 2024

0379-7112/© 2024 The Author(s). Published by Elsevier Ltd. This is an open access article under the CC BY license (<http://creativecommons.org/licenses/by/4.0/>).

The flammability studies of wood cylinders can be compartmentalized to two primary categories. The first category encompasses research that applies cylindrical wood rods as the resemblance of dead vegetation, to characterize the effects of fuel properties on wildland fires. For instance, in 1950, Fons [13] studied the rapid heating of pine wood cylinders to replicate forest fire scenarios. Effects of the specimens' initial temperature (10.0–65.5 °C), size (dia 0.238–0.635 cm), and moisture content (1.5–19.3%) on the ignition time were measured. In 2015, McAllister et al. [14] investigated the autoignition of red oak rods with diameters ranging from 0.64 to 1.91 cm under a convective-dominant heating scenario. The sample rods were heated with a hot air stream inside a specifically designed apparatus. They employed an infrared camera to measure the ignition time and location, as well as the surface temperature of the rods at the ignition moment. In 2019, Lin et al. [7] measured the piloted ignition delay time and ignition temperature of wood rods (dia 0.32–1.59 cm) in three fuel layouts that are commonly found in wildland fires: a single rod in vertical alignment, a single rod in horizontal alignment, and a rod bed in horizontal alignment. Experiments on the vertical alignment were conducted in a vertical Pyrex tube heated with halogen lamps, whereas horizontal measurements were carried out in a cone calorimeter. They argued that the traditional categorization of thermally thin and thick for flat fuels may not be suitable for cylindrical wildland fuels due to the intensified convection around curved surfaces.

Wood rods have also been used in experiments as surrogates for electrical cables because they possess similar charring properties but are physically more robust and well-behaving. Studies of Mangs [15] and Mangs and Hostikka [16,17] measured the vertical flame spread rate on 2.0 m long Birch rods in a custom flame spread apparatus. This problem was also numerically modeled using Direct Numerical Simulation (DNS) [17] and Large Eddy Simulation (LES) [18] methods. The cylindrical sample modeling was treated as axisymmetric in both approaches, which is in accordance with the physics of the problem. However, cylindrical objects in cone calorimeter experiments, if placed perpendicular to the radiative heat flux vector, as usual, cannot be modeled axisymmetrically due to non-uniform heat flux exposure on the sample. While the top side of the cylinder is exposed to radiation from the heater, the curvature of the cylinder causes a variation of incident surface heat flux from top to bottom. The bottom side of the cylinder normally touches the insulation material serving as a substrate. This non-uniformity of the heat flux exposure on the sample requires more accurate geometrical modeling.

In our prior work [12], we introduced a novel numerical technique for modeling the detailed radiative and convective heat fluxes and sample deformation during a cone calorimeter experiment of cylindrical objects. This approach incorporates a realistic representation of cylindrical samples and models the actual geometry of the conical heater. The solid-phase solution relies on two-dimensional heat transfer and pyrolysis methods. We validated this simulation framework using Poly(methyl methacrylate) (PMMA) cylinders, which are representative of non-charring materials, and provided the angular profiles of heat fluxes in the early stages of the pyrolysis. Due to the sample deformation (consumption), it was not possible to export sample surface heat fluxes from times beyond the ignition. The current study investigates the ability of the modeling framework [12] to predict the fire performance of *charring* cylindrical objects. We first construct a two-dimensional pyrolysis model for Birch rods and validate it using both gasification and flaming experiments. We determine and describe the geometrically-induced non-uniformities that arise in cone calorimetry measurements of charring polymers. We estimate incident and convective heat flux angular distributions on the surface of the charring cylindrical specimens for times before ignition and beyond. Finally, a simplified expression of these heat flux distributions, intended for ease of use in practical engineering modelings, is provided.

2. Experimental methods

2.1. Material selection

Birch wood (*Betula pendula*) in the form of cylindrical rods with a measured diameter of 20.0 ± 0.1 mm were utilized in this study. The rods were cut into 95.0 ± 0.2 mm long samples and conditioned at 20 °C and 45% relative humidity. Moisture content of the material was measured 8% wet basis, determined by weighing the mass loss of rods after being dried completely in a 105 °C oven. Dry density of the material was measured 534 ± 9 kg m⁻³ with a 95% confidence interval, calculated by weighing 55 sample rods and assuming the aforementioned moisture content.

2.2. Gram-scale experiments

An ISO 5660 standard cone calorimeter was utilized to assess the flammability of the Birch rods under both gasification and flaming conditions. To perform gasification tests, the chamber was purged with Nitrogen to maintain an atmosphere with less than 1% Oxygen concentration. Flaming measurements were fed with open air passing through the chamber gills. Entire experiments were performed at a radiation level of 50 kW m⁻², calibrated with a fluxmeter 25 mm away from the cone plate, where it corresponds to the top of the central rod on the sample holder.

Measurements were conducted in two sets: (1) Only one wood rod placed at the center of the sample holder, and (2) the whole 10 cm × 10 cm-area of the holder covered with five rods next to one another. Measurements were continued until all of the material was charred and no obvious pyrolyzate gas was visible, after which slow smoldering of the char was noted in flaming cases. This phase of the tests is not reported in the mass loss rate (MLR) and heat release rate (HRR) results. Three repetitions per configuration were performed. The MLR and HRR curves are reported as an arithmetic mean of the repetitions (smoothed by a 10-point moving average method for a more perceptive data presentation) and 95% confidence interval, computed as double the time-averaged standard deviation.

Videos were recorded from the cross-sectional pyrolysis of the rods with a DSLR camera through the glass door of the test chamber, and with a thermal camera (FLIR A655sc) through a small Calcium Fluoride Crystal window installed on the glass door. Snapshots of the DSLR-camera recordings served as the reference for a qualitative comparison against model predictions for char-front propagation. The thermal camera recordings were used only to provide insights on the selection of proper modeling boundary conditions for the wool substrate under the samples.

3. Numerical methods

The simulations were carried out with the FDS software [19], release version 6.7.9. It is a Computational Fluid Dynamics (CFD) solver for fire-driven flows with necessary submodels for the gas-phase flow, combustion and heat transfer, as well as the condense-phase heat transfer and decomposition reactions. This section describes the applied solid-phase algorithms in the current study. For details of each algorithm, the reader is referred to [20].

3.1. Pyrolysis reaction model

The pyrolysis reaction model obeys the mass conservation between the gaseous pyrolyzates and the condensed phase [20]. Multiple simultaneous reactions may occur in a material component, and each of these reactions may produce other solid components (residues) and gaseous species. The mass per unit volume of the component α , $\rho_{s,\alpha}$, is solved by:

$$\frac{\partial \rho_{s,\alpha}}{\partial t} = - \sum_{\beta=1}^{N_{r,\alpha}} r_{\alpha\beta} + S_{\alpha} \quad (1)$$

where $N_{r,\alpha}$ is the number of reactions for material α , $r_{\alpha\beta}$ is the rate of reaction β , and S_{α} is the production rate of component α due to the reactions of the other components. The reaction rate, $r_{\alpha\beta}$, is based on Arrhenius function:

$$r_{\alpha\beta} = A_{\alpha\beta} \rho_{s,\alpha}^{n_{s,\alpha\beta}} \exp\left(-\frac{E_{\alpha\beta}}{RT_s}\right) \quad (2)$$

where $A_{\alpha\beta}$ is the pre-exponent factor, $E_{\alpha\beta}$ is the activation energy, and $n_{s,\alpha\beta}$ is the reaction order of the reaction β of the component α . R and T_s are the universal gas constant and solid temperature, respectively. It should be noted that no gas transfer is assumed inside the solid phase, meaning that gaseous productions are discharged instantaneously to the gas phase.

Wood is a composite material made of Cellulose, hemicellulose (Pentosans), lignin, and extractives, with different proportions [21,22]. As for modeling purposes, various reaction schemes are introduced in the literature. For engineering applications, the primary components are usually taken into account during pyrolysis modeling, meaning that the extractives are often neglected. Broidio-Shafizade pyrolysis scheme was originally introduced for modeling the decomposition of cellulosic materials [23]. It assumes that the condensed phase first degrades into an active solid with a reduced degree of polymerization. The active material then decomposes with two competitive reactions, yielding, respectively, (a) char and gaseous species in lower temperatures, and (b) volatile tar in higher temperatures. Di Blasi [24] applied the Broidio-Shafizade reaction scheme for modeling the lignocellulosic (lumped Cellulose and hemicellulose species together) particles of wood since it forms about 75% of the wood components. Koufopoulos et al. [25] suggested that each primary component of the wood can undergo a Broidio-Shafizade reaction separately, and the wood degradation would be a linear superposition of cellulose, hemicellulose, and lignin decompositions. Gronli et al. [26] discovered through their measurements that it is sufficient to simulate the microscale pyrolysis of wood using a one-step reaction for each primary component of the wood. The most simple scheme for wood pyrolysis is a one-step reaction, known as the Antal scheme [27], which is defined as the direct transformation of wood into char and gaseous yields. The Antal scheme, or the modified version of it where the evaporation of water content to water vapor is also considered, has been applied to model various problems due to ease of usage and adequate precision, for example, [17,28–35].

For modeling the pyrolysis of Birch, Hostikka and Matala [29] applied the Broidio-shafizade, Gronli, and Antal schemes, while modifying each scheme to include the evaporation of moisture content as well. They concluded that the predictive capability of the simple, single-step reaction mechanism for the reproduction of gram-scale measurements is equally good as that of the more complex mechanisms. Thus, the single-step pyrolysis model introduced by them is utilized herein to avoid both introducing unnecessary complexities and increasing computational cost.

Fig. 1 represents the adopted reaction path and the corresponding kinetic parameters. Hostikka et al. [29] firstly used the built-in analytical optimization method of FDS [19] to estimate model kinetic parameters for each of their TGA experiments individually, i.e. measurements with heating rates of 2, 5, 10, and 20 °C min⁻¹. Then they generalized the parameters for arbitrary heating rates by averaging over the activation energies, and finding a corresponding pre-exponential value. Here, we utilized the parameter set for the dry Birch estimated in [29]. However, the moisture evaporation parameters were estimated with the built-in TGA analysis solver of FDS with a visual comparison of the numerical results against experiments. This has been carried out to improve the fitting of the current model to the reference measurements only for the water evaporation reaction. Eventually, the used parameter set is $A_{11} = 5.58 \cdot 10^7 \text{ s}^{-1}$, $E_{11} = 1.23 \cdot 10^2 \text{ kJ mol}^{-1}$, $n_{s,11} = 1.0$, $A_{21} = 4.0 \cdot 10^4 \text{ s}^{-1}$, $E_{21} = 4.79 \cdot 10^1 \text{ kJ mol}^{-1}$,

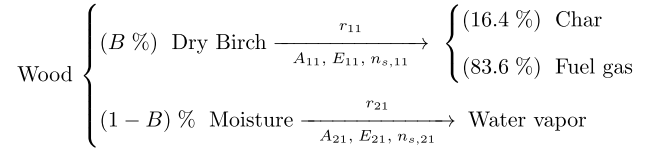


Fig. 1. Utilized degradation path of the Birch wood [29].

$n_{s,21} = 1.0$. B is the initial percentile of the dry birch component in TGA experiments. Hostikka and Matala reported B values to be 97.3, 96.4, 97.4, and 98.4 for heating rates of 2, 5, 10, and 20 °C min⁻¹, respectively. They made use of an averaged percentile for the Char and Fuel gas yields over the four TGA heating rates, thus we applied the same values in the current study.

The performance of the adopted kinetic reaction is illustrated in Fig. 2 by comparing the simulated TGA mass (Fig. a) and mass loss rate (Fig. b) against measurements of Hostikka et al. [29] for different heating rates. The model specifically focuses on predicting the MLR peaks at the temperatures at which the peaks occur. Nevertheless, it is not capable of reproducing the shoulder of the MLR curve starting around 250 °C, as it was also observed in [29].

The current TGA modeling approach targets the occurrence temperature at which the peak of the mass loss rate curve happens, which we recall as the *peak TGA* approach. An alternative approach to the TGA modeling can be developed to target the onset temperature of the shoulders of the decomposition reaction rather than its peak's occurrence temperature. Such a scheme is referred to as the *onset TGA* approach, detailed in Appendix A. In practice, the onset TGA approach shifts the predictions towards lower temperature by 35 °C, i.e. advancing the initiation of the main pyrolysis reaction. The influence of opting for this TGA approach on the cone calorimetry prediction is detailed in Appendix A, and briefly discussed in Section 4.3.

3.2. 2D heat transfer and pyrolysis algorithms

Solid heat transfer

Eq. (3) describes the governing physics of heat transfer within the condensed phase. On the left-hand side, T_s denotes the temperature, while ρ_s and c_s are density and specific heat of the solid, respectively. The right-hand side includes the divergence of the heat flux vector, \mathbf{q}'' , and the rate of change of the volumetric heat source due to pyrolysis reactions, \dot{q}_s''' .

$$\rho_s c_s \frac{\partial T_s}{\partial t} = -\nabla \cdot \mathbf{q}'' + \dot{q}_s''' \quad (3)$$

The equation is discretized by a Finite Volume Method. The mean temperature and pyrolysis heat source are assigned to the center of a solid cell, whereas the heat flux vector, \mathbf{q}'' , is computed at the center of a cell face, using the first-order discretization of Fourier's law. For instance, at time level n in x direction:

$$\dot{q}_{s,i+\frac{1}{2}}'' = -k_{s,i} \frac{T_{s,i+\frac{1}{2}}^n - T_{s,i}^n}{\frac{1}{2} \delta x_i} = -k_{s,i+1} \frac{T_{s,i+1}^n - T_{s,i+\frac{1}{2}}^n}{\frac{1}{2} \delta x_{i+1}} \quad (4)$$

where $i + \frac{1}{2}$ is the face center for cell indices i and $i + 1$, and k_s is the thermal conductivity. Thermal properties at face centers are calculated by linear averaging. For example, the cell interface temperature $T_{s,i+\frac{1}{2}}^n = (T_{s,i}^n + T_{s,i+1}^n)/2$.

Boundary treatments of solid heat transfer model

The boundary condition on the surface of the solid material follows the continuity of heat flux:

$$-k_s \frac{\partial T_s}{\partial x} = \dot{q}_{r,in}'' - \dot{q}_{r,out}'' + \dot{q}_c'' \quad (5)$$

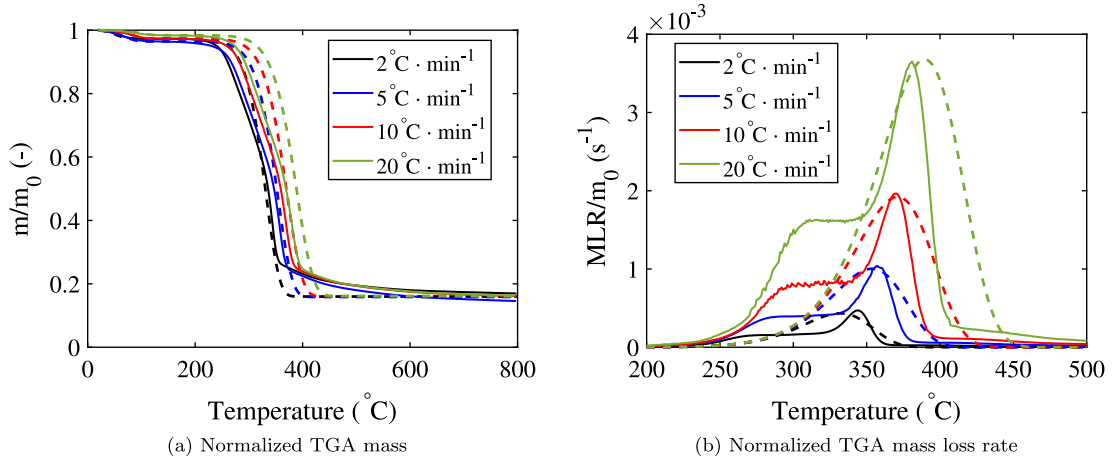


Fig. 2. Comparison of experimental (solid lines) [29] and current simulation (dashed lines) of thermogravimetric analysis of the birch sample for various heating rates. (For interpretation of the references to color in this figure legend, the reader is referred to the web version of this article.)

where $\dot{q}_{r,in}''$ and $\dot{q}_{r,out}''$ are the absorbed and emitted radiative fluxes at the solid surface, and \dot{q}_c'' is the convective flux. Note that in the current study, we do not consider in-depth radiation.

$\dot{q}_{r,in}''$ is calculated by the gas phase radiation solver. Thermal radiation in the gas phase is solved by a finite volume method, assuming a gray, non-scattering gas. To initiate each simulation, the RadCal narrow-band model generates look-up tables for temperature-dependent gray absorption coefficients for all involved gases, i.e. fuel, water vapor, carbon dioxide, and soot. Throughout the simulation, these tables are used to retrieve absorption coefficients, which are then added up based on the instantaneous volume fractions within each cell. A path length of 0.1 m is used in the computation of absorption coefficients. The CFD gridding is utilized for the spatial discretization of the radiation transport equation, and the solid angle is divided into 60 control angles [20]. In computing the emission source terms, it is assumed that the temperature and concentration fields are well resolved by the 1 mm mesh size. Thus, the emission power is predicted through the instantaneous absorption coefficient and temperature.

$\dot{q}_{r,out}''$ is calculated from the predicted wall temperature, T_w :

$$\dot{q}_{r,out}'' = \epsilon \sigma T_w^4 \quad (6)$$

where σ is the Stefan-Boltzmann constant for black bodies.

The convective flux is applied to the horizontal and vertical surfaces of the surrogate Birch cylinder(s) that come into contact with the gas phase. The convective flux is modeled with Newton's law of cooling, $\dot{q}_c'' = h(T_g - T_w)$, where T_g represents the gas temperature at the center of the first off-wall gas-phase cell. The heat transfer coefficient, h , is derived from a blend of empirical correlations for both natural and free convection [20,36]:

$$h = \frac{k}{L} \max(\text{Nu}_{\text{free}}, \text{Nu}_{\text{forced}}) \quad \text{W}/(\text{m}^2 \text{K}) \quad (7)$$

where L represents a characteristic length scale $L = 0.02$ m, taken as the cylinder's diameter. The Nusselt number, Nu , is dependent on the geometric and flow characteristics. Free convection is a function of Rayleigh number, Ra :

$$\text{Nu}_{\text{free}} = \begin{cases} (0.825 + 0.324 \text{Ra}^{1/6})^2 & \text{Vertical faces} \\ 0.54 \text{Ra}^{1/4} & \text{Horizontal faces, } \text{Ra} \leq 10^7 \\ 0.15 \text{Ra}^{1/3} & \text{Horizontal faces, } \text{Ra} > 10^7 \end{cases} \quad (8)$$

and forced convection is a function of Reynolds, Re , and Prandtl, Pr , numbers:

$$\text{Nu}_{\text{forced}} = (0.037 \text{Re}^{0.8} - 871) \text{Pr}^{1/3} \quad (9)$$

The Prandtl number is assumed to be $\text{Pr} = 0.7$. Reynolds number is calculated as $\text{Re} = \rho |\mathbf{u}| L / \mu$, where \mathbf{u} is the first off-wall flow velocity and μ is dynamic viscosity.

In the authors' earlier study [12], it became evident that the model is insensitive to varying the L from 2 cm to 10 cm, or assigning both vertical and horizontal surfaces the same heat transfer coefficient of $h = 10 \text{ W}/(\text{m}^2 \text{K})$. Moreover, the pyrolyzate gas that blows out of the solid boundaries may influence the convective fluxes (blowing), which is not directly considered in this study.

Pyrolysis algorithm

In each computational cell, the sample wood is a mixture of three solid material components: moisture, dry Birch, and char. The time evolution of the bulk density of each component is computed by Eq. (1). The total density of the solid cell in each time step is the sum of the densities of those three components, $\rho_s \equiv \sum_{\alpha} \rho_{s,\alpha}$.

The movement of the pyrolyzate gas through the material is assumed to be instantaneous, ignoring the finite diffusivity, flow resistance, and material anisotropy. The pyrolysis volatiles appear at the nearest wall cell as a mass flux boundary condition to the gas phase. Pyrolyzed gas produced by more than one solid cells below the surface may eject from a particular wall cell. For a row of cells in the x direction tied to the wall cell w , the mass flux generation of pyrolysis gas component γ is computed by:

$$\dot{m}_{\gamma,w}'' = \sum_{i \in w} \dot{m}_{\gamma,i,k}'' \delta x_i \quad (10)$$

where δx_i represents cell width, and $\dot{m}_{\gamma,i,k}''$ is the rate of mass generation per unit area for the pyrolyzate component γ .

3.3. Cone calorimetry model setup

The calorimeter chamber modeling is based on the 2D setup utilized in our earlier study [12]. It was shown that this 2D model not only can provide equally good results as its 3D counterpart but also is at least 10 times computationally less demanding. For the sake of brevity, a summary of the setup is explained hereunder.

The Birch cylindrical cross sections were numerically approximated with attaching multiple $1 \times 1 \text{ mm}^2$ solid obstructions. The same thermo-physical and optical properties of the mineral wool substrate as in [12] was utilized in here too, i.e. $\rho = 128 \text{ kg m}^{-3}$, $k_s = 0.1 \text{ W m}^{-1} \text{K}^{-1}$, $c_s = 1 \text{ kJ kg}^{-1} \text{K}^{-1}$, and $\epsilon = 0.9$. The substrate temperature was predicted with a one-dimensional heat conduction model in flaming simulations, whereas in non-flaming cases, fixed surface temperatures of 450°C and 200°C were applied for single and five rods simulations, respectively. The latter boundary conditions were indicated experimentally with the thermal camera while performing O_2 -free measurements. The exteriors were set to an open boundary condition, feeding the domain with air or pure Nitrogen in the flaming or non-flaming cases, respectively.

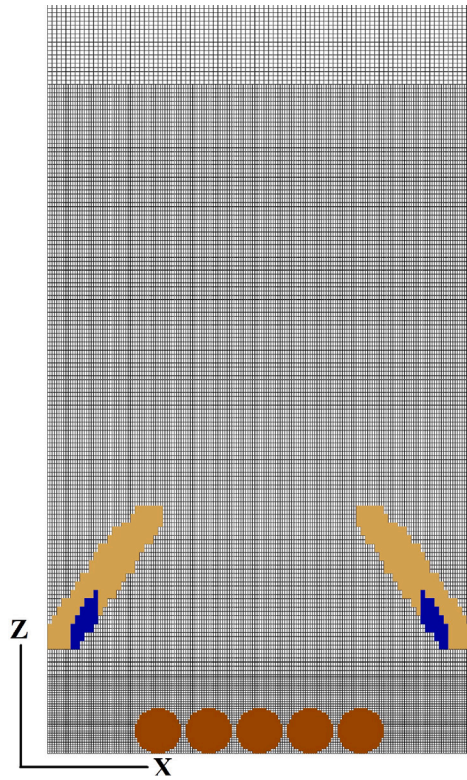


Fig. 3. 2D Solution domain along with the presence of five Birch rods.

The modified 2D cone heater geometry of [12] was used in the current work, presented for the five rods flaming scenario in Fig. 3. The geometrical modification refers to a reduction of 12 mm of the width of the heater elements in each direction, shown in blue color, to ensure a correct incident radiative flux distribution despite the 2D approximation. Validation of a truthful radiative flux distribution on the top point of the rods was performed in [12]. Three separate cell sizes were used for different locations of the solution domain: $\Delta x = \Delta z = 1$ mm in the vicinity of the rods; $\Delta x = 1$ mm and $\Delta z = 1.875$ mm in the vicinity of the heater; and $\Delta x = 2$ mm and $\Delta z = 1.875$ mm far above the heater. The latter region was only necessary for five rods flaming case, partly visible on top of Fig. 3, where long flames were obtained. The computational time was reduced by dividing the domain into 7, 11, and 13 grids in gasification, single rod flaming, and five rods flaming simulations, and sending each grid to a separate MPI (Message Passing Interface) process.

Due to the high geometrical complexity and the associated computational cost of the model, it was not possible to optimize the thermophysical parameters using the current measured data. Instead, a carefully selected set of parameters was drawn from the existing literature on Birch or hardwood slabs, ensuring the attainment of reasonable predictions. Table 1 represents a summary of modeling parameters, along with their corresponding references of data. Moisture properties were taken from [29], owing to the similar inclusion of moisture evaporation reaction in TGA modeling between the present work and the aforementioned reference. The Dry Birch and Char thermal parameters were taken from Chaos [32] who estimated these parameters through inverse modeling of the pyrolysis of hardwood pallets in an inert environment of the Fire Propagation Apparatus. The material properties obtained from their particular estimation approach can be applicable to other scenarios with spectrally different radiation sources than the FPA. Ding et al. [28] adopted these material properties of [32]

Table 1

Condensed phase thermophysical parameters used for Birch rod cone calorimetry simulations.

Parameter	Value	Ref.
Thermal conductivity ($\text{W m}^{-1} \text{K}^{-1}$)	$k_{\text{Birch}} = 0.26$	[28,32]
	$k_{\text{Moisture}} = 0.3$	[29]
	$k_{\text{Char}} = 0.36$	[28,32]
Specific heat ($\text{kJ kg}^{-1} \text{K}^{-1}$)	$c_{\text{Birch}} = 2.533$	[28,32]
	$c_{\text{Moisture}} = 4.3$	[29]
	$c_{\text{Char}} = 1.45$	[28,32]
Emissivity (–)	$\epsilon_{\text{Birch}} = 0.9$	[32]
	$\epsilon_{\text{Moisture}} = 1.0$	[29]
	$\epsilon_{\text{Char}} = 0.85$	[28,32]
Heat of Reaction (kJ kg^{-1})	$H_{r,\text{Birch}} = 300$	[29]
	$H_{r,\text{Moisture}} = 2260$	[29]
Heat of Combustion (kJ kg^{-1})	$H_c = 14350$	[18,29]
Density (kg m^{-3})	$\rho_{\text{Birch}} = 534$	Measured
	$\rho_{\text{Moisture}} = 1000$	[29]
	$\rho_{\text{Char}} = 120$	[29]

to simulate the pyrolysis of wet Birch under cone calorimetry in air atmosphere and demonstrated the validity of the parameters. Moreover, the reaction scheme, illustrated in Fig. 1, closely resembles that of [29]. Consequently, the heats of reactions are sourced from [29]. Model sensitivity to thermophysical parameters is detailed in Appendix A and briefly explained in Section 4.3.

3.4. Combustion and turbulence models

The pyrolyzate gas is assumed to be $\text{C}_{3.4}\text{H}_{6.2}\text{O}_{2.5}$, as it was suggested by Ritchie et al. [37] for the decomposition of Birch. The fuel combusts in the air with a global one-step reaction $\text{Fuel} + \text{Air} \rightarrow \text{Products}$, producing 1% soot and 14.35 MJ kg^{-1} heat. Assuming infinitely-fast chemistry, the Eddy Dissipation Concept [38] is used for modeling the mass combustion rate within a cell with initial fuel and air mass fractions Y_F and Y_A , respectively:

$$\dot{m}_F''' = -\rho \frac{\min(Y_F, Y_A/s)}{\tau_{\text{mix}}} \quad (11)$$

where ρ is the cell mass density, and s is the mass stoichiometric coefficient of air. The characteristic mixing time, τ_{mix} , relies on the local state of the flow field and considers the time scales associated with chemical reactions, molecular diffusion, subgrid-scale advection, and buoyant acceleration [20]. Then the local heat release rate is calculated by multiplying the \dot{m}_F''' and the heat of combustion, H_c .

For turbulence modeling, the LES mode of the FDS is used, as against the Very Large Eddy Simulation (VLES) mode, since detailed information of the CFD solution is targetted in this study. The Deardorff turbulent viscosity model [39] is applied everywhere except near walls. The WALE model of Nicoud and Ducros [40] is utilized for the eddy viscosity calculations in the first off-wall grid cells, to correctly apply the no-slip condition on the solid walls. The reader is referred to [20] for details of these models.

4. Results and discussion

4.1. Gasification cone calorimetry

The current section evaluates the accuracy of the model in predicting the mass loss rate of the gasification measurements using the peak TGA scheme and thermal properties shown in Table 1. Fig. 4 compares the simulation results for single- and five-rod setups against the experimental data, where the shaded area represents the 95% confidence interval of the experimental data. In the single-rod case, the time

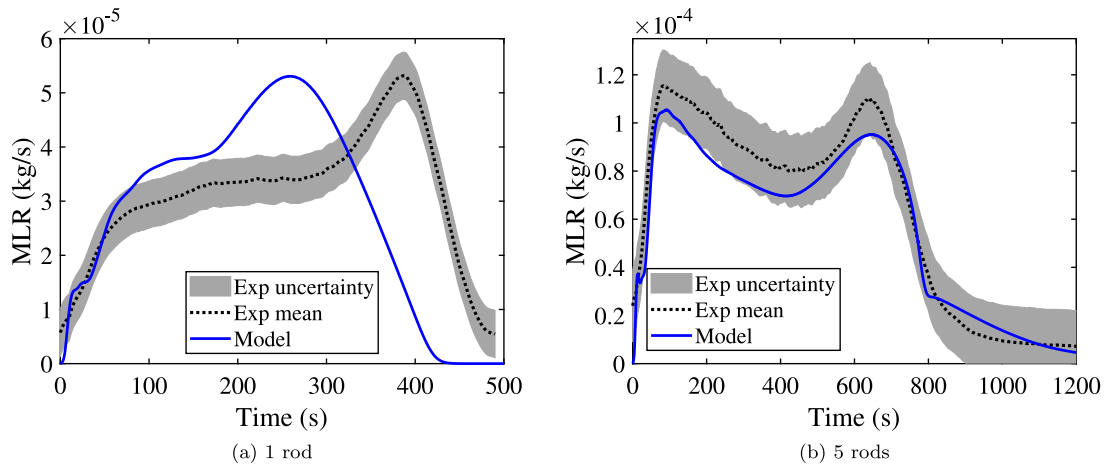


Fig. 4. Comparison of mass loss rates between experimental and model prediction for single and five-rod gasification test cases.

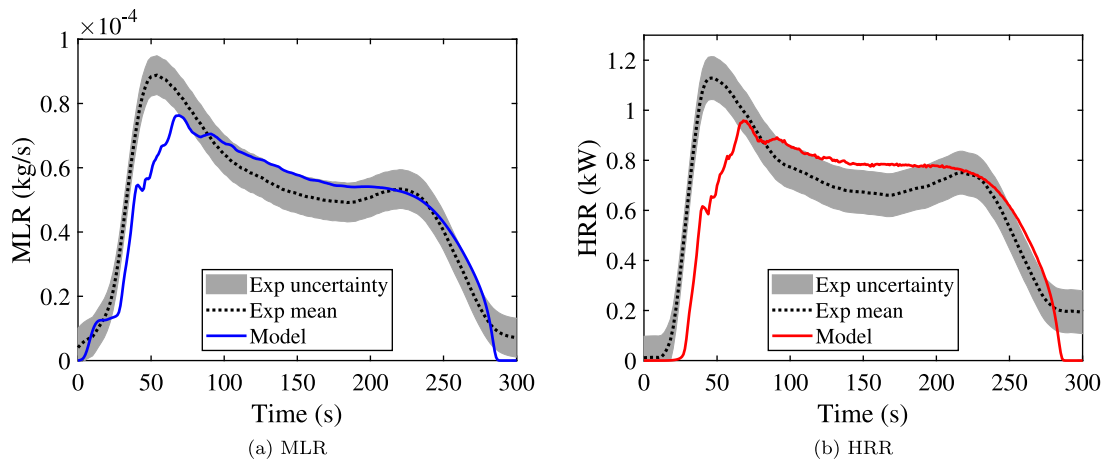


Fig. 5. Comparison of mass loss and heat release rates between experimental and model prediction for single rod flaming test case.

series shows only one pyrolysis peak, which appears close to the end of the test, whereas the five-rod case shows a classic two-peak shape. The model predicts the main pyrolysis peak of the one-rod case about 130 s earlier than the measurements, while for the five-rod case, the MLR peaks are predicted in a more accurate temporal alignment to the experimental data. Potential reason can be the geometrical similarity between the tight, five rods sample alignment and the slab samples used for obtaining the thermophysical parameters (Table 1), in contrast to the single-rod case where the non-rectangular effect has a greater role.

4.2. Flaming cone calorimetry

Here we assess the ability of the 2D model to reproduce MLR and HRR of the single-rod and five-rod flaming measurements. Fig. 5 presents the results for the single rod case. Experimental data show a main peak for both MLR and HRR right after ignition, at about 55 s, followed by a decaying trend until a slightly intensified decomposition rate between 200–240 s occurs. The model captures the main peak and the decaying trend after that, but fails to reproduce the second peak. The MLR prediction in Fig. 5(a) shows a 15 s delay in the numerical prediction of the first peak, however, the difference of the area under the numerical and experimental mean curves is within 1% accuracy. The main peak of the HRR prediction in Fig. 5(b) denotes a 22 s delay compared to the peak occurrence time of the measurements. The area under the simulated HRR curve is underpredicted by 13.8% in comparison to that of the experimental mean curve.

Fig. 6 presents the results for the five-rod flaming case. Experimental measurements show a single peak, followed by a decaying trend. The model predicts the time of the first peak very well but generates another peak at the simulation time of about 500 s. The areas under the simulated MLR and HRR curves are underpredicted by 11.1% and 25.5%, respectively. Such a relatively large HRR underprediction was also observed in our previous work with PMMA rods [12].

Possible causes for the HRR under-prediction include the approximations in the combustion and radiation modeling, such as the single-step, mixing-controlled reaction scheme and the lack of detailed soot model, and the use of literature values for the thermophysical parameters. These potential causes warrant further investigation in future research. However, the favorable prediction of the temporal decomposition of the material inside the cross-section of the condensed phase, demonstrated in the upcoming Section 4.4, indicates a reasonably modeled thermal environment at the fuel surface. Therefore, we can conclude that despite the observed uncertainties in MLR and HRR predictions, the model captures most of the key features of the gasification and flaming pyrolysis that are important for this study. Hence, we rely on the current model as a source of thermal environment characteristics at the sample surface, discussed later in Section 4.5.

4.3. Summary of model sensitivity

Before exploiting the model for the thermal environment characterization, it is good to understand the influence of the input and modeling uncertainties on model predictions. A brief deduction on the model

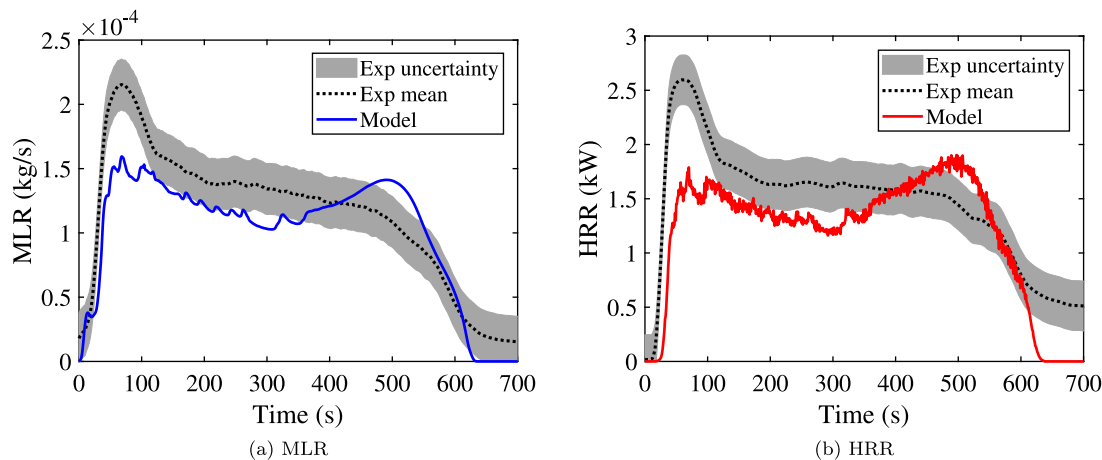


Fig. 6. Comparison of mass loss and heat release rates between experimental and model prediction for five rods flaming test case.

sensitivity analysis against the choice of TGA modeling, numerical resolution, and thermophysical parameters is described hereunder, whereas a detailed analysis is expanded upon in [Appendix A](#). The sensitivity study is only performed on the single rod flaming simulation.

As mentioned in Section 3.1 the choice of the onset TGA versus peak TGA scheme may influence the initiation of the birch degradation process. Simulation with the onset TGA scheme leads to a slight time advancement and amplitude increment of the MLR peak prediction. However, both TGA models seem to be viable methods to apply.

Performing a simulation with 0.5-mm grid resolution in the vicinity of the condensed phase showed insignificant changes in the MLR prediction compared to that of the original 1-mm resolution, but a fourfold increase of the simulation time. Moreover, as described in Section 3.3, a coarser mesh resolution has been used in the areas farther away from the condensed phase. To investigate the sensitivity of the HRR prediction to the grid spacing in these areas, another simulation was performed with a uniformly distributed 1-mm grinding everywhere in the domain. Although the computation time increased almost threefold, no substantial alteration was noted in either MLR or HRR predictions. Thus, it is concluded that the original grid generation described in Section 3.3 satisfies the mesh independency target.

To assess the model's sensitivity to the thermophysical parameters tabulated in [Table 1](#), simulations were conducted by varying the values of these parameters by $\pm 20\%$. Results demonstrated that increasing birch conductivity delays ignition and accelerates burnout, while an increase in char conductivity leads to faster burnout. The findings underscore the importance of considering both birch and char conductivities in predictive pyrolysis models for charring cylinders. Varying birch's specific heat by 20% has a more pronounced effect on the model prediction than similar changes in conductivity. Increasing c_{Birch} results in delayed and reduced amplitude of the MLR peak prediction, while a 20% reduction of c_{Birch} improves peak timing and amplitude but causes an unfavorably advanced burnout prediction. The model is insensitive to changes in c_{Char} . Increasing the emissivity of virgin birch slightly advances ignition and the MLR peak predictions, and vice versa. Alteration of the char emissivity has no impact on the MLR prediction. An elevation of 20% in H_r leads to a prediction with a slight decline in the amplitude of the main MLR peak and a modest delay in the burnout time, whereas the results with a 20%-reduced heat of reaction manifests an opposing trend.

4.4. Char front propagation

In this section, a qualitative evaluation of the precision of the 2D model is conducted through a comparison of the char front's evolution

in experimental and simulated scenarios. Selected snapshots from the experimental video recordings, chosen to aptly depict the propagation pattern of the char front, are compared with corresponding simulation slices of char density.

[Fig. 7](#) shows a sequence of snapshots that depict the measurements of single rod gasification for $t = 50$ s to 400 s. The process initiates from the top surface, with the charred wood becoming visible at the end of the rod. The images indicate that the char front tends to move from top to bottom at a faster pace than from the sides to the center. This phenomenon occurs due to the fact that the radiation view factors between the heater and the points located on the top surface are higher than to the points on the lower rod surface. A similar observation has also been made in [\[12\]](#) in the same measurement setup but with a non-charring rod, where the top-to-bottom material shrinkage was more pronounced than the side-to-center shrinkage. The simulation slices presented on the right-hand side of [Fig. 7](#) display a similar pattern; the model can predict the shape and area of the remaining virgin wood (non-red cells) relatively well.

Apart from the char front propagation, [Fig. 7](#) shows that, with the passage of time, pyrolysis leads to a reduction in the rod's thickness by altering the curvature of the top surfaces, eventually leading to a slightly flatter shape. The current model is not able to reproduce such a deformation because the birch-to-char conversion ratio is constant, and because the possible char oxidation and burn-away are not modeled.

[Fig. 8](#) presents a comparison between measurement snapshots and FDS char density slices at various times for the single rod flaming case. The flame originates at the top of the rod, which is apparent in the snapshot captured at $t = 30$ s. The flame edge progressively tilts towards the lower sections of the rod surface and reaches the wool substrate in a few tens of seconds, as evidenced by the snapshot for $t = 55$ s. The char front penetrates into the rod from both top-to-bottom and sides-to-center directions at comparable rates, consistent with the observations reported in [\[12\]](#) for the shrinkage of a non-charring rod. The more rapid decomposition of the sides compared to the gasification case in [Fig. 7](#) is attributed to the increased heat transfer resulting from the presence of the flame on the rod's sides. The simulation slices displayed on the right-hand side of [Fig. 8](#) affirm the model's capability to accurately replicate this degradation pattern in a timely manner.

In [Fig. 9](#), the char front propagation of the five-rod gasification case is illustrated. The measurement snapshots on the left-hand side indicate that the initial decomposing regions mainly include the top surface of the three central rods and the inner surfaces of the two outermost rods, as observed at $t = 90$ and 250 s. The experiment reveals a U-shaped trend of char front penetration over time, again consistent with the findings reported in [\[12\]](#). This trend is partly attributed to the reduction

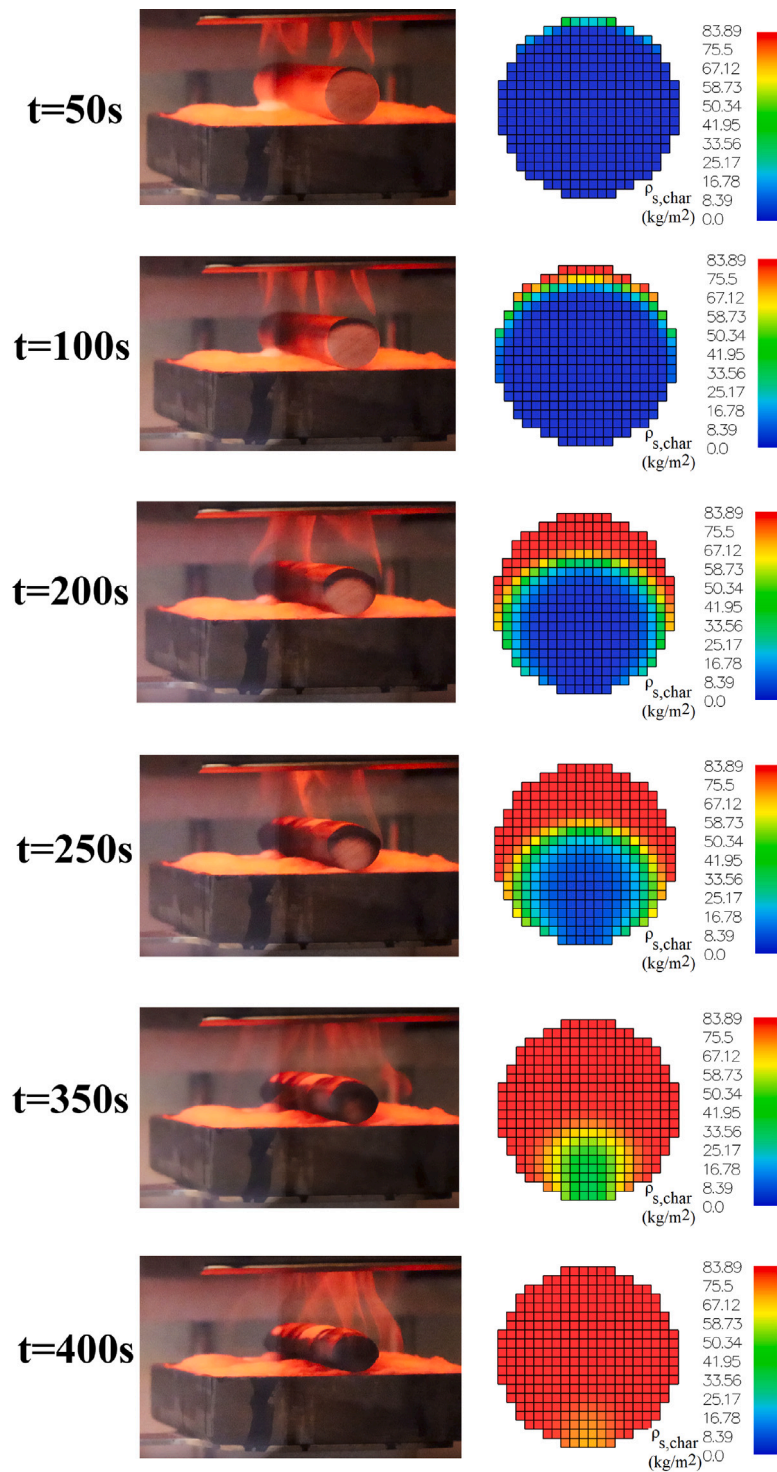


Fig. 7. Comparison of experimental (left) and numerical (right) char front propagation on the sample cross-section at different times of the single rod gasification experiment. Color bar represents the cell density of the char component. (For interpretation of the references to color in this figure legend, the reader is referred to the web version of this article.)

in the heater-produced incident flux when moving from the center of the sample holder to its sides. However, the principal cause of this U-shaped trend is the varying view angles at which the two outermost rods perceive the heater radiation, in contrast to the other rods. For instance, the local heater-to-sample view factor is larger for the western half of the rightmost rod than for its eastern half, thereby enhancing the heating of the western half. At $t = 800$ s, the three central rods are nearly fully charred, while virgin wood is still visible in the outer areas

of the outermost rods. During the last few minutes of the measurements, the rods began to bend upward and crack due to thermal expansion, as observed at $t = 1100$ s. The numerical results displayed on the right-hand side of Fig. 9 demonstrate that the model accurately reproduces the U-shaped trend of the char front propagation.

A sequence of recorded and predicted cross-section images from the five rods flaming case is illustrated in Fig. 10. In the measurements, the ignition of the flame occurs at the top of the rods, as demonstrated

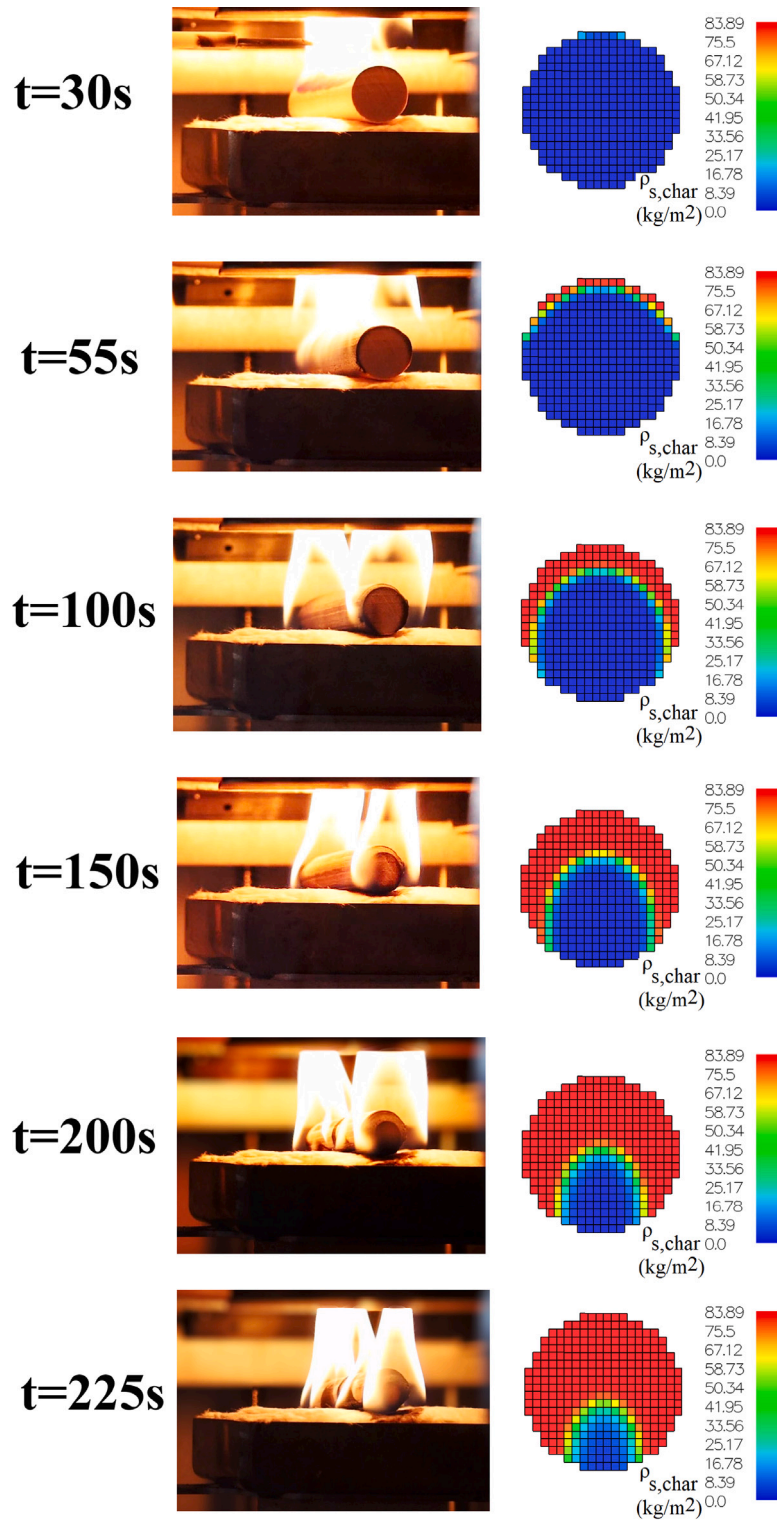


Fig. 8. Comparison of experimental (left) and numerical (right) char front propagation on the sample cross-section at different times of the single rod flaming experiment. Color bar represents the cell density of the char component. (For interpretation of the references to color in this figure legend, the reader is referred to the web version of this article.)

by the snapshot at $t = 70$ s, and subsequently propagates downwards along the lower surface of the outermost rods until it reaches the wool substrate, as indicated by the snapshot at $t = 200$ s. Taking the rightmost rod as an example, the existence of the flame on the eastern circumference intensifies the local heat transfer compared to its western half. This uneven distribution leads to a \cap -shaped char front profile on the top of the samples. This phenomenon is consistent with the

previous findings reported in [12], where a similar trend was observed for the shrinkage of non-charring rods under the same experimental conditions. The snapshot at $t = 550$ s indicates that the outermost rods experience a faster degradation rate compared to the three central rods due to the uneven heating profile, leading to the early depletion of virgin material in the outermost rods. The remaining virgin material in the central rods continues to decompose, maintaining flames in this

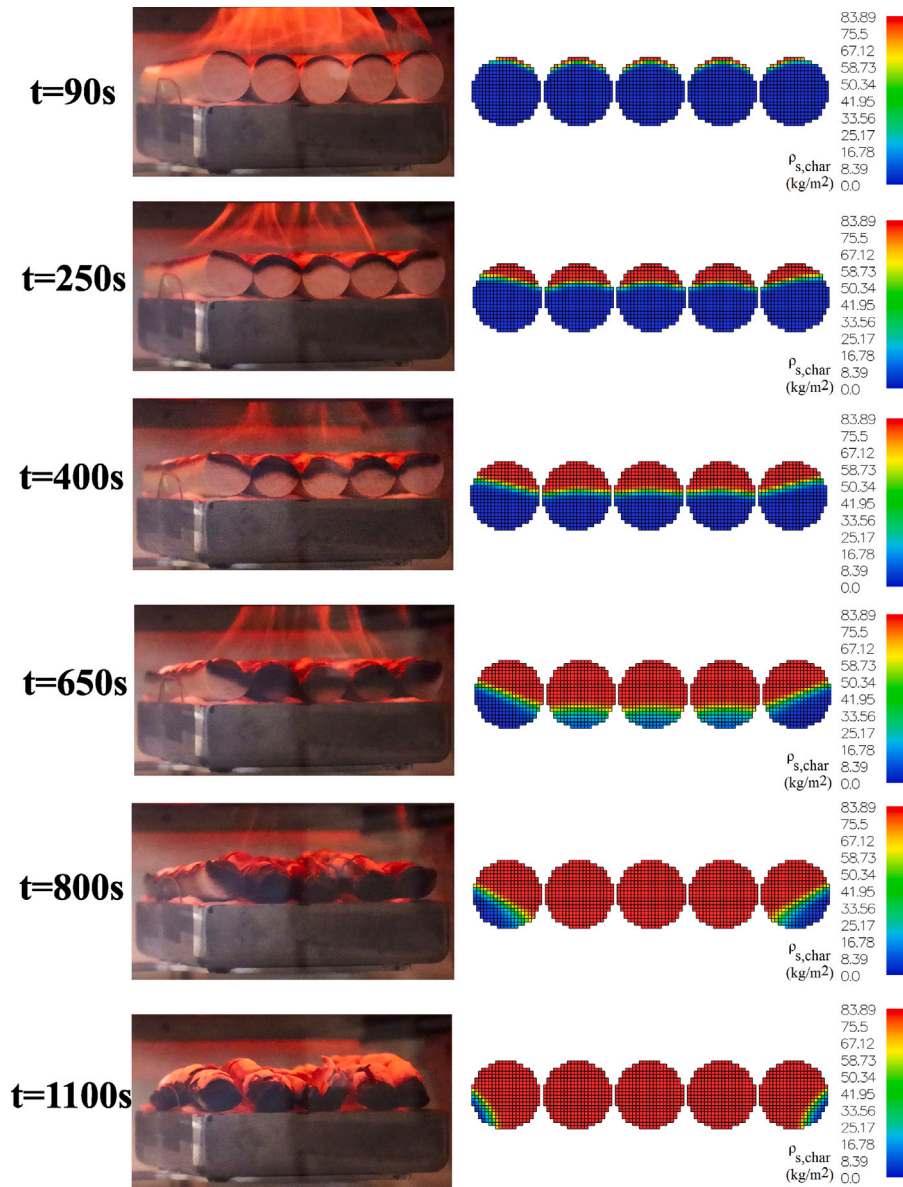


Fig. 9. Comparison of experimental (left) and numerical (right) char front propagation on the sample cross-section at different times of the five rods gasification experiment. Color bar represents the cell density of the char component. (For interpretation of the references to color in this figure legend, the reader is referred to the web version of this article.)

region. The FDS slices of char density on the right-hand side of Fig. 10 demonstrate that the 2D model predicts the \cap -shaped profile of the char front propagation accurately in terms of timing and the remaining area of the virgin material.

4.5. Predicted surface quantities

The preceding section provided a qualitative discussion of the factors underlying the various observed degradation patterns in each scenario. In this section, these factors are quantitatively analyzed on the sample surfaces. The boundary heat fluxes are reported exclusively for the surfaces of the central and rightmost rods in this investigation. To facilitate clarity of presentation, the data is plotted only for the rightmost halves of the rods under examination. The fluxes are obtained at distinct simulation times for both the gasification and flaming scenarios, with an emphasis on selecting times that exhibit common or similar features in both environments. This approach enables the elucidation of the reasons behind the differences in char front patterns observed between the different cases.

Fig. 11 compares the surface fluxes for the single rod gasification and flaming cases. The incident radiative heat flux and convective heat flux distributions are represented by solid and dashed lines, respectively. The gasification case is presented in Fig. 11(a), where the $t = 2$ s curves display the initial distribution of fluxes on the rod. The nominal 50 kW m^{-2} incident heat flux is observed on the top of the rod, while it decreases to 0 kW m^{-2} on the bottom point of the rod. As time progresses, the incident heat flux distribution remains almost unchanged. The initial convective heat flux distribution at $t = 2$ s indicates negligible convection, except for a small convective heating region between 140° to 180° angles, which is due to the Nitrogen stream flowing over the wool substrate and being heated by the hot wool surface before reaching the sample rod. At later simulation times (i.e., $t = 30$ – 100 s), the upper half of the rod experiences slight convective cooling due to the flow of surrounding Nitrogen. However, the small convective heating region on the lower surfaces remains active with the same magnitude as at the beginning of the simulation. The gradual reduction of the incident heat flux along the rod circumference, while the convection remains relatively negligible, explains the relatively higher top-to-bottom char propagation described in Section 4.4.

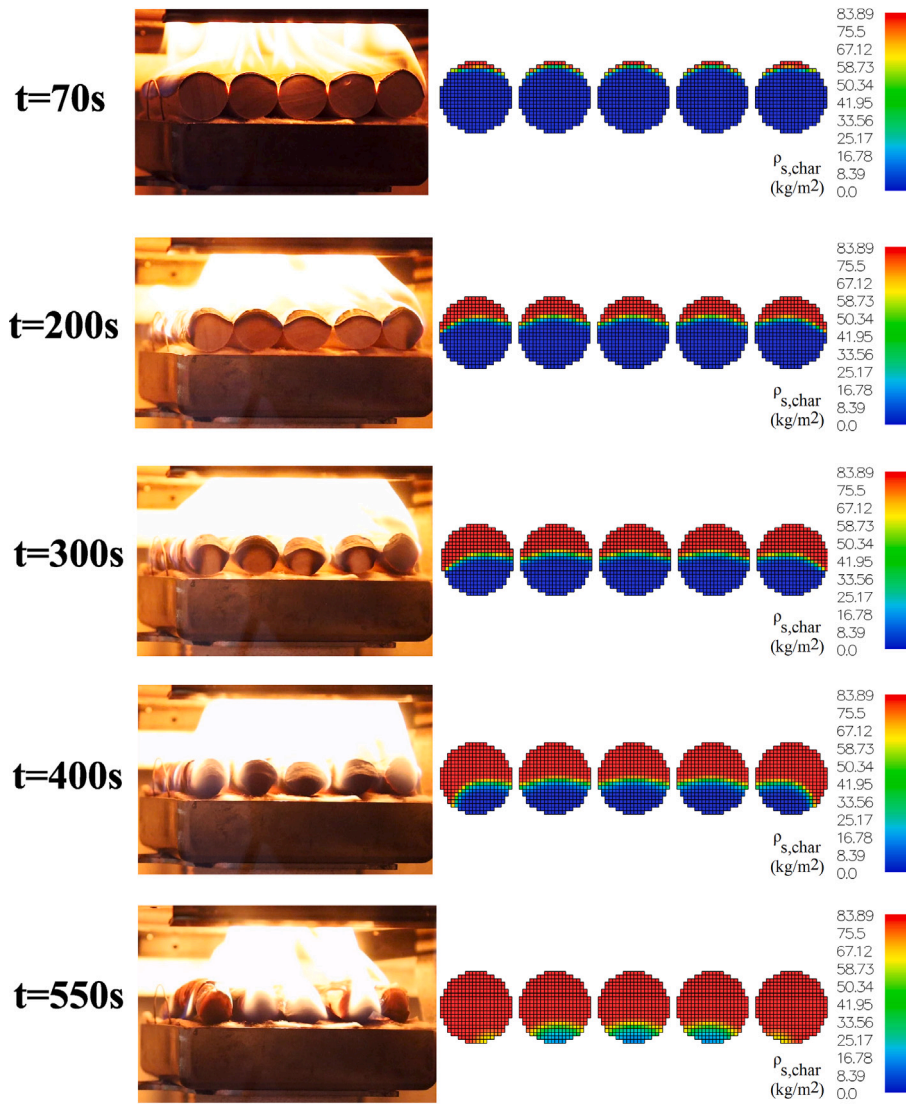


Fig. 10. Comparison of experimental (left) and numerical (right) char front propagation on the sample cross-section at different times of the five rods flaming experiment. Color bar represents the cell density of the char component. (For interpretation of the references to color in this figure legend, the reader is referred to the web version of this article.)

In Fig. 11(b), the flux predictions for the single rod flaming case are presented. The initial incident heat flux distribution is comparable to that observed during gasification at $t = 2$ s. Upon ignition of the flame at the top of the rod at $t = 30$ s, the incident flux predominantly increases in the middle portions of the circumference, with an augmentation of about 10 kW m^{-2} . At $t = 50$ s, the same augmentation in the incident flux affects the upper part of the circumference. Comparison between the incident flux distribution at $t = 100$ s and $t = 2$ s reveals that the incident flux at the top of the rod remains approximately 10 kW m^{-2} greater than its initial value. However, the existence of the flame on the rod's sides leads to an increase of approximately 15 kW m^{-2} for most of the circumference's other locations. The initial convective fluxes are very small, similar to the gasification case. With the ignition at the rod's top at $t = 30$ s, a local sudden increase of the convection is observed. As revealed by the curve at $t = 50$ s, the convection wave moves along the rod surface as the flame edge descends. At $t = 100$ s, the flame's location has become steady with no further movement of the flame edge. The convective flux distribution exhibits a bell curve with a maximum value of $+15 \text{ kW m}^{-2}$ located at the midpoint of the circumference. These flame-induced increases in both incident and convective fluxes on the side of the rod explain the intensified side-to-center char propagation in comparison to the gasification case.

Fig. 12 compares the heat flux distributions for the five-rod gasification and flaming cases. The solid lines in the figure depict the heat flux data for the central rod, whereas the dashed lines represent the heat flux distributions for the rightmost rod.

Considering the incident heat flux results for the gasification case shown in Fig. 12(a), the top of the central rod is consistently exposed to the calibrated incident flux of 50 kW m^{-2} , while it decreases to zero moving from the top towards the lateral position (Angle = 90°). Comparison of the flux distribution with that of the single rod case in Fig. 11(a) reveals a steeper slope of the decrease, which is attributed to the shadowing effect of the adjacent rods on the central rod. Over the simulation time interval of $t = 2$ s to 100 s, the increased temperature of the neighboring rods results in an increased incident heat flux, primarily on the upper half of the central rod's circumference. At $t = 400$ s, about 10 kW m^{-2} increase of incident flux, compared to the initial state, can be seen on the entire upper circumference. The overall heating of the rods increases the incident heat flux also at 100° to 180° circumferential angles, although the charring has only progressed to about halfway through the rod thickness at $t = 400$ s. When comes to the rightmost rod, the incident heat fluxes on its eastern half remain relatively constant throughout the simulation period. The flux values for this rod are generally lower than those of the central rod, owing to the lower heater-to-sample view factors.

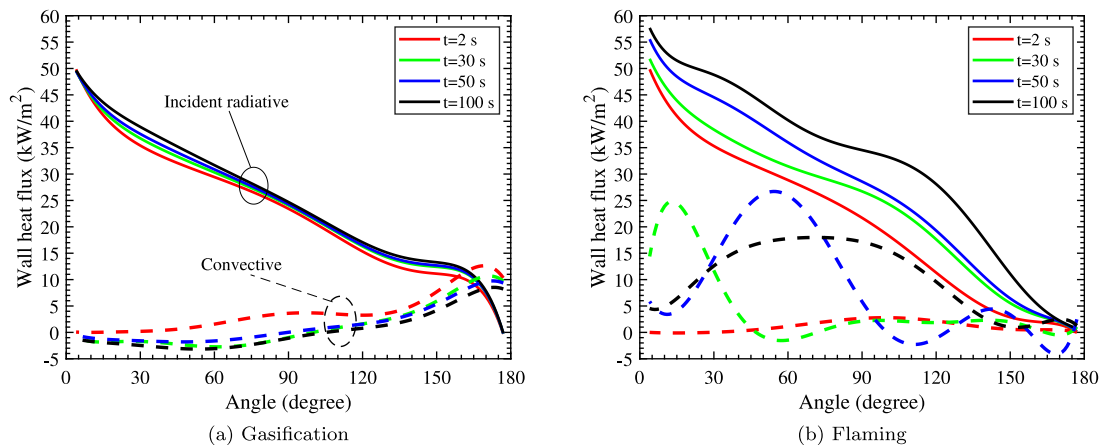


Fig. 11. Simulated heat fluxes at the sample surface for the single rod gasification and flaming cases. Solid lines represent incident heat flux distribution, whereas dashed lines show the distribution of convective heat flux. (For interpretation of the references to color in this figure legend, the reader is referred to the web version of this article.)

The convective heat fluxes from the five-rod gasification scenario are depicted in Fig. 12(b). The central rod displays a negligible amount of convective heating, whereas the upper perimeter of the eastern half of the rightmost rod experiences convective cooling throughout the entire simulation. This cooling phenomenon is attributed to the Nitrogen flow in the vicinity of the outermost samples. However, the magnitude of the convective heat flux remains considerably lower than that of the radiative incident flux. The observed U-shaped trend earlier is attributed (mostly) to the gradual increase of the radiative heating in central regions and (to some extent) the convective cooling experienced by the outer rods.

The results from Fig. 12(c) reveal that, in the flaming case, the incident radiative flux distributions at pre-ignition times (i.e., $t = 2$ and 30 s) are similar to those observed in the gasification case. However, post-ignition, the flame considerably enhances the magnitude of the incident flux for the upper half of the circumference of the central rod, with the top point experiencing an increase of about 10 kW m^{-2} . As in the five-rod gasification case, the elevated temperature of the adjacent rods promotes a re-radiation effect towards the surface of the central rod, leading to an augmented incident flux around the circumference over time, as evidenced by the distribution at $t = 400$ s. This phenomenon, in conjunction with the flame-induced radiation, leads to an increase of nearly 20 kW m^{-2} in incident flux at angles ranging from 10° to 100° along the circumference of the central rod. At later time, $t = 400$ s, the observed incident heat flux at $100^\circ < \text{Angle} < 180^\circ$, i.e. within the cavity between rods and the substrate, is about 6 kW m^{-2} , which corresponds to about 300°C surface temperatures.

For the rightmost rod, the flame-induced increase in the incident flux of about 10 kW m^{-2} is evident on its upper half post-ignition, i.e. at $t = 50, 100$, and 400 s. As discussed in Section 4.4, the flame edge tilts towards the lower circumference of the eastern half of the rod with the passage of time. Furthermore, the virgin material present on the upper half of the rod undergoes complete decomposition over a period. Thus, the active pyrolysis and combustion region shifts gradually towards the lower parts of the rod during the simulation. The descent of the flame edge produces a wave of flame-induced incident flux that moves downwards towards the corresponding active pyrolysis area. This phenomenon is reflected in the dashed line for $t = 400$ s.

The convective flux distribution along the central rod in Fig. 12(d) is found to be nearly negligible throughout the simulation, except for a brief moment around the ignition time at $t = 30$ s, during which the convective flux on top of the rod reaches $+20 \text{ kW m}^{-2}$. This increase is short-lived and dissipates after ignition. In contrast, the rightmost rod displays a noticeable rise in convective flux on its top surface at $t = 30$ s with the initiation of the flame. As the simulation progresses, the flame grows stronger and propagates towards the lower circumference

of the rod, resulting in a distinct wave-like pattern in the convective flux distribution at $t = 50$ s. The flame-induced convective flux moves with the flame towards the lower circumference of the rod, where an active pyrolysis region is present, as evident from the convective flux distribution at $t = 100$ and 400 s. The maximum value of the flame-induced convective flux on the eastern half of the rightmost rod (after the flame stabilizes) is approximately 30 kW m^{-2} , three times greater than the flame-induced incident flux. However, their regions of effectiveness are different. The flame-induced convection is influential at $0^\circ < \text{Angle} < 150^\circ$ range, while flame-induced radiation is more effective in the $100^\circ < \text{Angle} < 180^\circ$ range (compare dashed lines for $t = 400$ s in Fig. 12(c) and (d)). The enhanced convective heating and radiation on the outermost rods result in the \cap -shaped charring profile observed in Section 4.4.

4.6. Summary of heat fluxes on cylindrical objects in gasification and cone calorimetry

The gas phase domain serves two primary functions: a) it transports radiation from the heater elements to the solid surface, and b) it provides the heat feedback from the gas surrounding the samples to the solid surfaces. By eliminating the necessity of solving the CFD domain and focusing only on the solid phase domain, simulation costs and complexities could be significantly reduced for an engineering model.

In Section 4.5, surface quantities across the cylindrical samples' circumference were examined, presenting detailed heat flux distributions. However, implementing such intricate flux distributions, which vary both temporally and angularly, can be laborious in engineering modeling practices. To enhance practical usability, these distributions are summarized herein to offer a more straightforward approach. The simplified heat flux distributions are elaborated upon in the subsequent discussion and presented explicitly in Tables 2–4 for the single rod cases, central rod within the five rods configuration, and the rightmost rod of the five rods cases, respectively.

With a reasonable approximation, the radiation received at the surface solely due to the cone's emission remains constant throughout the tests, independent of time. To simplify the analysis, one can exclude the conical heater and its radiation transfer within the gas and only consider their overall effect, i.e. "Initial incident radiative flux distribution". These distributions are depicted as polar plots for the right halves of the central cylinders in the first columns of tables. Note that, for the convenience of the modeler, the initial incident flux distribution on the rightmost rod, Table 4, is presented exactly the same as that of the central rod in Table 3, even though they differ in reality. This discrepancy is compensated by introducing a corrective feedback radiative flux, as elaborated below.

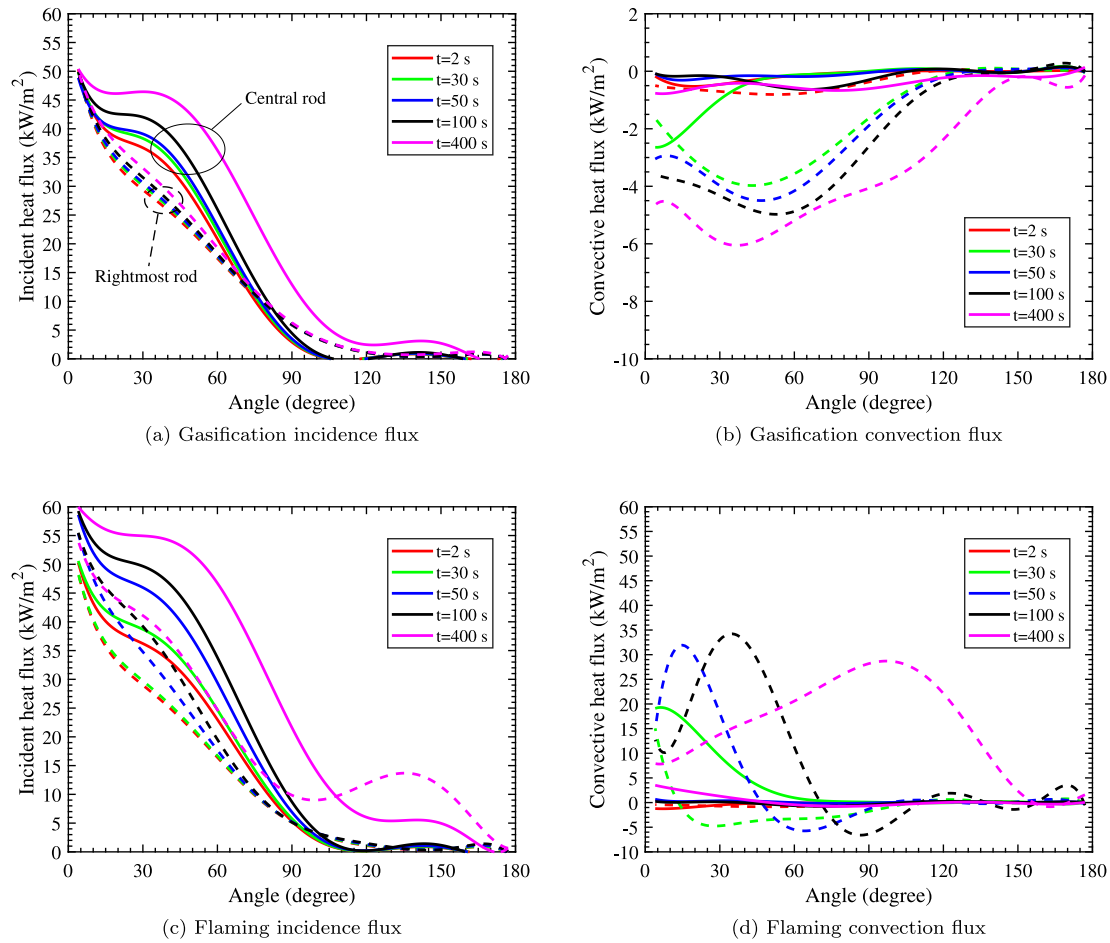


Fig. 12. Simulated heat fluxes at the sample surface for the five rods gasification and flaming cases. Solid lines represent data for the central rod, whereas dashed lines show the distributions on the rightmost rod. (For interpretation of the references to color in this figure legend, the reader is referred to the web version of this article.)

Similarly, the heat feedback from the gas phase to the samples' surface can be replaced with the combined effects of convective and radiative feedback along the circumference. However, these feedback mechanisms are time-dependent. By synthesizing the insights derived from the MLR analyses in Sections 4.1 and 4.2, the char penetration paths discussed in Section 4.4, and the alterations in heat flux outlined in Section 4.5, distinct *time frames* emerge, each playing a determinative role in the degradation process.

The MLR evolution of the single rod gasification case indicates a “Growth” stage when the degradation begins to escalate rapidly (for example, the time interval when $1 \times 10^{-5} < \text{MLR} < 3.5 \times 10^{-5} \text{ kg s}^{-1}$). This Growth time frame in the single rod flaming case occurs only after an “Ignition” interval. Subsequently, both single rod cases experience a “Peaking” region. However, the analysis of the char front transformation indicates that there are no significant changes in the penetration path for both cases after the “Peaking” period. Consequently, the heat flux distributions likely remain relatively stable post-peaking. In summary, for the single rod cases, we delineate three distinct chronological time frames presented in Table 2: “Ignition”, “Growth”, and “Peaking”. Nonetheless, the situation for the five rods cases is slightly different.

Analysis of the MLR evolutions in the five rods gasification and flaming cases shows that the time to reach the first peak is very short in both environments. Specifically in the flaming case, the transition from the Ignition to Growth periods occurs so quickly that it led us to merge both intervals into a single “Growth” interval. On the other hand, the char front analysis for both cases revealed slow and extended periods with slow charring, denoted here as “Plateau”. To summarize, we define the chronological time frames for the five rods cases as

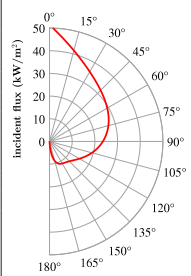
“Growth”, “Peaking”, and “Plateau”, shown in Tables 3 and 4. Notably, in Table 4, there is an additional column for the “Initial” time frame. This column specifies the required modification for the “Initial incident radiative flux distribution” used for the *central rod* (first column) to match the correct initial distribution for the current *rightmost rod*. This approach avoids the need for the introduction of a separate angular incident distribution specifically tailored for the rightmost rod, as the provided central rod distribution suffices. The correction is denoted in the row related to the radiative augmentation, which is valid across all time frames.

The changes of the radiative and convective heat fluxes from their initial angular distributions (Section 4.5) are extracted for each time frame and presented in the tables below. In specific cases, denoted by asterisks, the original, wave-like distribution has been approximated by a piecewise constant function. The combined effect of these convective and radiative augmentations is denoted as “Total” heat feedback from the gas phase to the sample surface.

Using the provided heat flux results, one can model the two-dimensional pyrolysis of charring cylinders without explicitly solving for the gas phase processes. This involves introducing cylindrical solid objects, applying the “Initial incident radiative flux distribution” as a continuous angular profile of external radiation, and then adding the “Total” gas phase feedback, corresponding to the specific angular position and simulation time frame. It is possible to interpolate or apply some smoothing to the piecewise constant distributions to remove artificial discontinuities.

Table 2

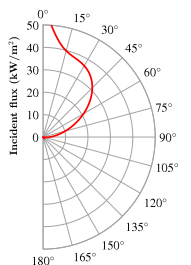
Heat flux augmentations for the single rod cases at three different time frames.

Initial incident radiative flux distribution	Time frame Flux type augmentation (kW · m ⁻²)	Ignition	Growth	Peaking
	Gasification			
	Radiative	N/A	0	0
	Convective	N/A	0° < θ < 90° : -3 140° < θ < 180° : +5	0° < θ < 90° : -3 140° < θ < 180° : +5
	Total	N/A	0° < θ < 90° : -3 140° < θ < 180° : +5	0° < θ < 90° : -3 140° < θ < 180° : +5
	Flaming			
	Radiative	60° < θ < 150° : +10	0° < θ < 150° : +10	0° < θ < 15° : +10 15° < θ < 150° : +15
	Convective	0° < θ < 30° : +15*	30° < θ < 90° : +15*	30° < θ < 120° : +15*
	Total	0° < θ < 30° : +15 60° < θ < 150° : +10	0° < θ < 30° : +10 30° < θ < 90° : +25 90° < θ < 150° : +10	0° < θ < 15° : +10 15° < θ < 30° : +15 30° < θ < 120° : +30 120° < θ < 150° : +15

* Original wave-like distribution has been approximated by piecewise constant function.

Table 3

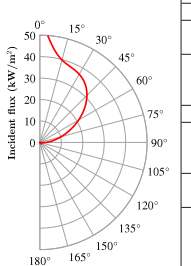
Heat flux augmentations for the central rod of a five-rod case at three different time frames.

Initial incident radiative flux distribution	Time frame Flux type augmentation (kW · m ⁻²)	Growth	Peaking	Plateau
	Gasification			
	Radiative	15° < θ < 100° : +2	15° < θ < 100° : +5	15° < θ < 100° : +10 100° < θ < 180° : +5
	Convective	0° < θ < 30° : -2	0	0
	Total	0° < θ < 15° : -2 30° < θ < 100° : +2	15° < θ < 100° : +5	15° < θ < 100° : +10 100° < θ < 180° : +5
	Flaming			
	Radiative	0° < θ < 100° : +10	10° < θ < 100° : +15	0° < θ < 10° : +10 10° < θ < 100° : +20 100° < θ < 180° : +6
	Convective	0° < θ < 30° : +20*	0	0
	Total	0° < θ < 30° : +30 30° < θ < 100° : +10	10° < θ < 100° : +15	0° < θ < 10° : +10 10° < θ < 100° : +20 100° < θ < 180° : +6

* Original wave-like distribution has been approximated by piecewise constant function.

Table 4

Heat flux augmentations for the rightmost rod of a five-rod case at four different time frames.

Initial incident radiative flux distribution	Time frame Flux type augmentation (kW · m ⁻²)	Initial	Growth	Peaking	Plateau
	Gasification				
	Radiative		15° < θ < 75° : -5		
	Convective	0		0° < θ < 120° : -3*	
	Total	15° < θ < 75° : -5		0° < θ < 15° : -3 15° < θ < 75° : -8 75° < θ < 120° : -3	
	Flaming				
	Radiative		15° < θ < 75° : -5		
		0	0° < θ < 15° : +5 0° < θ < 15° : +5	0° < θ < 45° : +5 90° < θ < 180° : +15	
	Convective	0	0° < θ < 45° : +20*	0° < θ < 75° : +20*	0° < θ < 150° : +20*
	Total	15° < θ < 75° : -5	0° < θ < 15° : +25 15° < θ < 45° : +15 45° < θ < 75° : -5	0° < θ < 15° : +25 15° < θ < 75° : +20	0° < θ < 15° : +25 15° < θ < 45° : +20 45° < θ < 75° : +15 75° < θ < 90° : +20 90° < θ < 150° : +35 150° < θ < 180° : +15

* Original wave-like distribution has been approximated by piecewise constant function.

5. Conclusions

Despite the ISO 5660 cone calorimeter being originally designed for the flammability assessment of rectangular, flat samples of construction materials, it has been increasingly applied to cylindrical polymeric fuels like electrical cables and wooden rods. Using the obtained experimental data for pyrolysis modeling has been problematic due to limited information regarding the heat exposure experienced by the cylindrical samples. Researchers conventionally simplify the analysis

by modeling rectangular volume replicas of cylindrical samples with 1D pyrolysis and heat transfer algorithms, neglecting surface heat flux heterogeneity, thus leading to increased modeling uncertainties. In our prior work [12], we introduced a novel 2D framework for modeling cylindrical non-charring objects in a cone calorimeter. The current research applied the same framework for a charring polymer.

Gasification and flaming measurements under (nominally) 50 kW m⁻² irradiation level were performed using single-rod and five-rod layouts of Birch wood cylinders, representative of a charring polymer. The

experimental results indicate a faster pace of top-to-bottom char penetration, compared to side-to-center, on the cross-section of the single rod gasification case. For the single rod flaming case, the charring pace in both directions was comparable. A U-shaped char front profile was observed in the five-rod gasification test, whereas the five-rod flaming case showed a \cap -shaped trend. All of these observations were similar to the patterns witnessed in [12] for the shrinkage of non-charring rods under the same experimental conditions.

The proposed computational framework was utilized to simulate the experiments. The MLR and HRR predictions were validated against the measurements, demonstrating the capability to reproduce the observed trends and shapes of the experimental time series with relative uncertainties of 13.8% (under-prediction) for the total heat release from a single flaming rod, 11.1% and 25.5% (under-predictions) for the total mass loss and heat release from five flaming rods. The high error in HRR is associated with the solution inaccuracy of the gas phase combustion [12]. Moreover, the numerical predictions of the char-front propagation qualitatively reproduced the experimental observations.

The angular distributions of the radiative and convective heat fluxes over the surface of the cylindrical samples were extracted from the simulations. The primary deviation from the conditions obtained by flat samples is obviously the steep reduction of the incident radiation between the top and sides of the samples. Apart from this general trend, a significant increase in the incident heat flux was observed in the five-rod configuration on the sides of the central rod due to the adjacency of the neighboring rods with increasing surface temperatures. This local increase reached up to 10 and 20 kW m⁻² in gasification and flaming conditions, respectively. In the five rods flaming scenario, as the flame edge descended on the outermost rods, a downward-moving wave of convective and incident heat fluxes, with amplitudes of approximately 20 and 15 kW m⁻², was observed.

The detailed, time- and angle-dependent flux distribution results were simplified and tabulated for practical engineering modeling. The tabulated data comprises (a) an invariant angular distribution of initial incident radiative flux on the cylindrical objects' circumference and (b) a piecewise continuous angular augmentation of the total (radiative+convective) gas phase heat feedback to the cylinder surface. By utilizing these simplified heat exposures, one can model the 2D pyrolysis of charring cylinders without the need to solve the gas phase.

Future research should apply the numerical framework to model electrical cables, addressing their intricate multi-layer, multi-component geometry. Additionally, utilizing the simplified version of the flux distributions in conventional cone calorimetry modeling methods requires more investigation.

CRedit authorship contribution statement

Morteza Gholami Haghighi Fard: Investigation, Methodology, Validation, Visualization, Writing – original draft. **Simo Hostikka:** Conceptualization, Funding acquisition, Investigation, Supervision, Writing – review & editing.

Declaration of competing interest

The authors declare that they have no known competing financial interests or personal relationships that could have appeared to influence the work reported in this paper.

Data availability

Data will be made available on request.

Declaration of Generative AI and AI-assisted technologies in the writing process

During the preparation of this work the author(s) used ChatGPT by OpenAI in order to check and improve English language expressions. After using this tool/service, the author(s) reviewed and edited the content as needed and take(s) full responsibility for the content of the publication.

Acknowledgments

This study has been funded by the State Nuclear Waste Management Fund (VYR), Finland. The authors wish to acknowledge CSC – IT Center for Science, Finland, for computational resources.

Appendix A. Model sensitivity

This appendix examines the influence of the input and modeling uncertainties on cone calorimetry model predictions. The model's sensitivity to TGA modeling, numerical resolution, decomposition heat, and thermal parameters are evaluated. This sensitivity study is performed solely on the single-rod flaming scenario.

For the analysis of the sensitivity to the TGA modeling, here we introduce an alternative TGA scheme in contrast to the *peak TGA* approach used in Section 3.1. This model, referred as the *onset TGA* scheme, facilitates an earlier start of the main reaction, thereby approaching the onset temperatures of the shoulders of the experimental MLRs, while maintaining the MLR peak values as that of the *peak TGA* approach. The A_{11} and E_{11} parameters of Fig. 1 are re-estimated for the 10 °C min⁻¹ heating rate such that the model's main pyrolysis reaction initiates at the onset of the MLR shoulder at about 216 °C. The estimation was performed by applying the internal TGA estimation routine of the FDS, leading to $A_{11} = 2.44 \cdot 10^7$ s⁻¹ and $E_{11} = 1.12 \cdot 10^5$ kJ mol⁻¹. The same kinetic parameters, without any change, are also employed for modeling the other 2, 5, and 20 °C min⁻¹ heating rates. The results of the onset TGA model are illustrated in Fig. A.1. The peak's occurrence temperature has reduced by approximately 35°C for all heating rates compared to the *peak TGA* approach. The purpose of introducing this model is to explore the extent to which earlier initiation of the reaction in the TGA modeling can affect the gram-scale predictions, discussed as what follows.

The consequence of the chosen reaction target on the cone calorimetry simulation is demonstrated in Fig. A.2(a). The application of the onset TGA scheme leads to a primary MLR peak that is 9.6×10^{-6} kg s⁻¹ higher and occurs 13 s earlier than when using the original, i.e. *peak TGA* scheme. As the MLR between 100 and 200 s is also slightly higher, the burnout occurs earlier than in the experiment. Overall, both schemes seem to be viable options for bench-scale, i.e. cone calorimetry, modeling.

To assess the impact of the mesh resolution, a simulation was performed utilizing a spatial discretization of 0.5 mm, alongside a regeneration of the rod geometry with solid cells of dimension 0.5×0.5 mm². Consequently, an almost fourfold increase in the simulation time was observed. Fig. A.2(b) compares the MLR of the simulation with 0.5-mm resolution against that of the simulation with 1-mm grid spacing. With the 0.5-mm resolution, the ignition time remains unchanged, the main peak is smoothed slightly, and the fuel burnout is delayed by 7 s. These observations are consistent with our earlier study on non-charring rods [12]. The 1-mm resolution seems to provide convergent solutions for modeling both non-charring and charring materials in cone calorimeter.

Fig. A.3 illustrates the model sensitivity to the main thermal parameters. k and c were varied $\pm 20\%$ from the values in Table 1. The ϵ values were varied by increasing to unity and decreasing by 20%. The variation of these parameters was performed for both the birch and char components of the model.

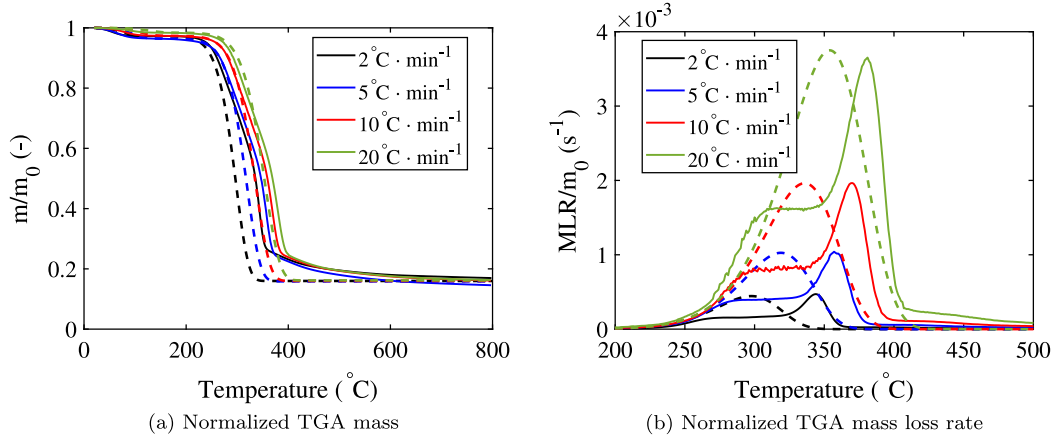


Fig. A.1. Modified Birch pyrolysis model for initiation of the main decomposition reaction at the onset of the peak. Solid lines present experimental results of [29]; dashed lines show the current model results. (For interpretation of the references to color in this figure legend, the reader is referred to the web version of this article.)

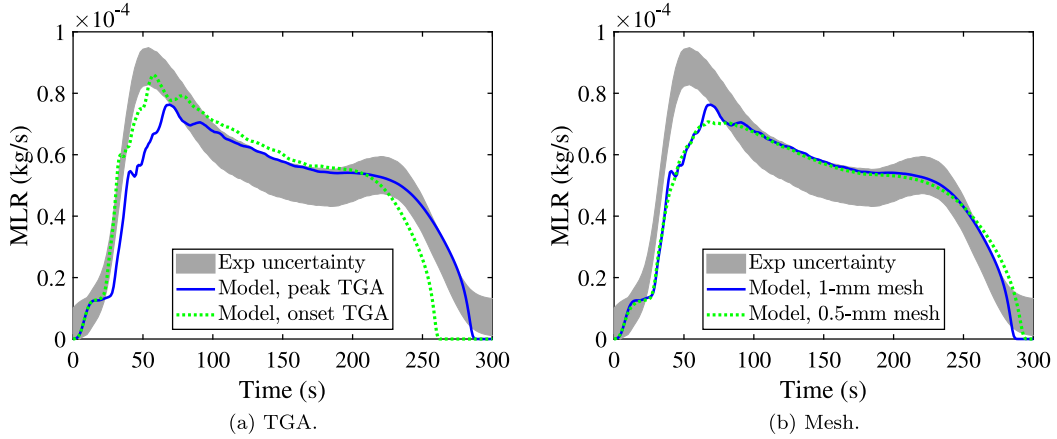


Fig. A.2. Sensitivity of the single rod flaming MLR to the TGA model selection and mesh resolution.

The results in Fig. A.3(a) and A.3(b) demonstrate a clear influence of birch and char conductivities on the pyrolysis process. An increase in k_{Birch} results in a delayed ignition, higher burning rate during the semi-steady state phase, and earlier burnout. This is in line with our previous study on non-charring rods [12]. Likewise, a 20% increase in k_{Char} (Fig. A.3(b)) leads to faster burnout. Reversely, decreasing the birch conductivity to $0.8k_{\text{Birch}}$ shifts the MLR peak to the left, while reducing the k_{Char} by 20% slightly decreases the amplitude of the MLR peak but does not change the peak's time of occurrence. These findings highlight the importance of considering the effects of both birch and char conductivities when developing predictive pyrolysis models for charring cylinders.

The model sensitivity to a 20% variation of the birch's specific heat is more prominent than that of the conductivity, which aligns well with a similar observation made in [12]. Fig. A.3(c) shows that while the model's result with the original c_{Birch} mostly falls within the experimental uncertainty bounds, increasing the specific heat to $1.2c_{\text{Birch}}$ results in both delay and amplitude reduction of the MLR peak. Conversely, reducing c_{Birch} by 20% leads to an improvement in the timing and amplitude of the main MLR peak, but the material burnout occurs 30 s earlier. Given these observations, the original value of c_{Birch}

appears to be a reasonable choice, as it results in the model being mostly within the uncertainty bounds. Furthermore, Fig. A.3(d) indicates that the model is insensitive to changes in c_{Char} . This observation can be attributed to the high conductivity of char, which facilitates heat transfer from the char layers on the outer layer of the rod to the virgin birch existing underneath the char layer. Additionally, as the density of char is much lower than that of birch, modest changes in char heat capacity do not significantly change its thermal inertia.

Increasing the emissivity of the virgin Birch to unity (Fig. A.3(e)) advances the ignition and the MLR peak by 7 s, whereas the MLR peak in the simulation with $0.8\epsilon_{\text{Birch}} = 0.72$ is delayed by 10 s. These trends are in line with the findings of [12]. As a consequence of the delayed ignition, the last stages of the MLR curve with $\epsilon_{\text{Birch}} = 0.72$ seem to fall outside of the experimental uncertainty bounds. Fig. A.3(f) shows that increasing the char emissivity to unity or decreasing it to $0.8\epsilon_{\text{Char}} = 0.68$ does not impact the MLR prediction. This is caused by the close-to-equilibrium state at the char surface where emissivity variations influence both absorbed (gained) and emitted (lost) radiation equivalently.

The sensitivity to the Birch heat of reaction was investigated as well (not shown for conciseness). A 20% increase of the H_r causes a

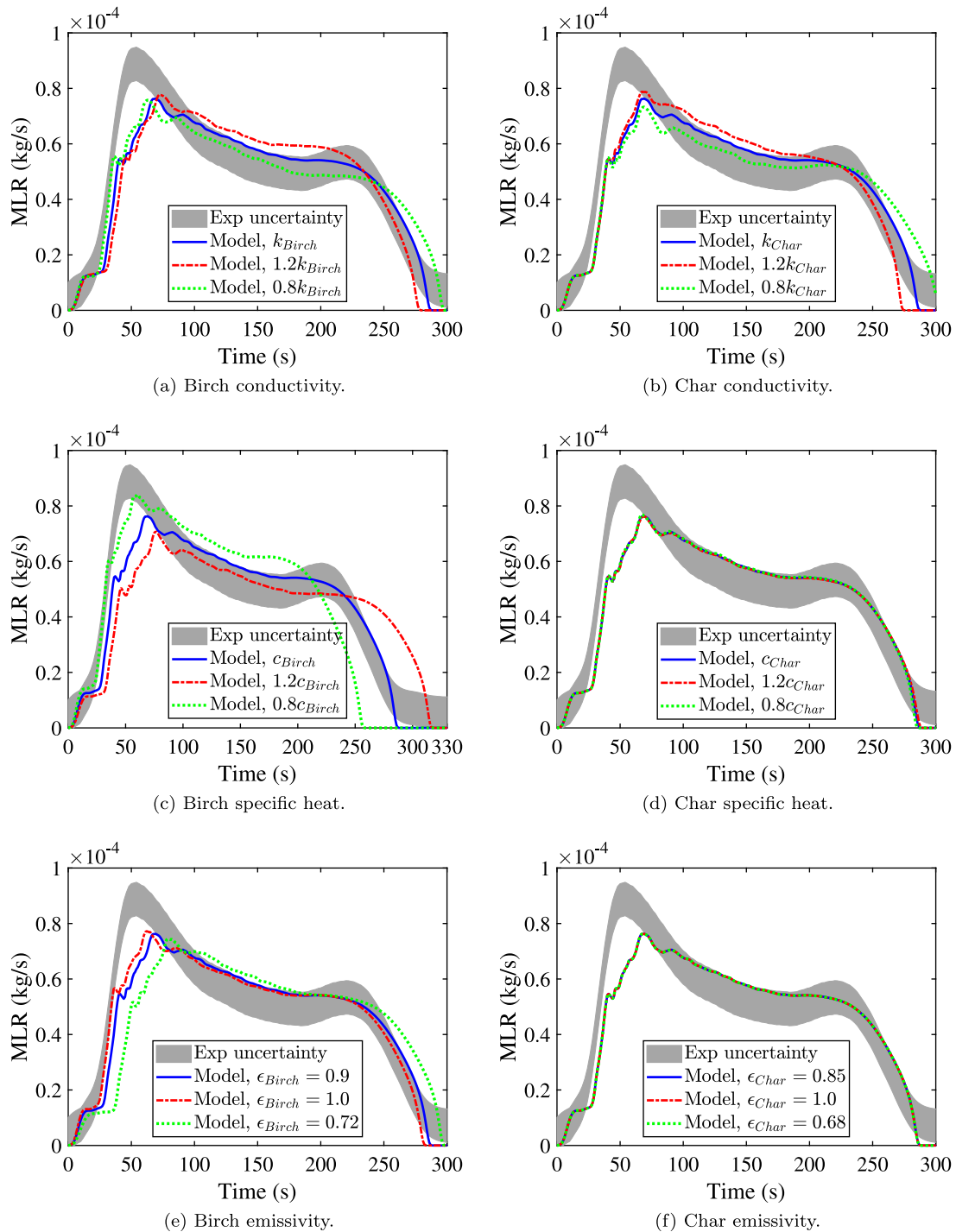


Fig. A.3. Sensitivity of the single rod flaming MLR to the thermal parameters. The model results with the original value (solid lines) are compared against the results with a 20% increase of the corresponding parameter (dash-dotted lines) and a 20% decrease of that (dotted lines). (For interpretation of the references to color in this figure legend, the reader is referred to the web version of this article.)

slight reduction in the amplitude of the main peak and a small delay in the burnout time, while the MLR result for $0.8H$, shows the other way around. The current deduction is in line with [12].

References

- [1] A. Standard, E2058, Standard Test Methods for Measurement of Material Flammability Using a Fire Propagation Apparatus (FPA), Technical Report, West Conshohocken, PA, 2013.
- [2] X. Liu, Design and Analysis of New Gasification Apparatus Based on the Standard Cone Calorimeter, University of Maryland, College Park, 2012.
- [3] J.D. Swann, Y. Ding, M.B. McKinnon, S.I. Stoliarov, Controlled atmosphere pyrolysis apparatus II (CAPA II): A new tool for analysis of pyrolysis of charring and intumescent polymers, *Fire Saf. J.* 91 (2017) 130–139.
- [4] Reaction-To-Fire Tests — Heat Release, Smoke Production and Mass Loss Rate — Part 1: Heat Release Rate (Cone Calorimeter Method) and Smoke Production Rate (Dynamic Measurement), ISO 5660-1:2015.
- [5] M. Ahrens, Home Structure Fires, National Fire Protection Association, 2007.
- [6] O. Keski-Rahkonen, J. Mangs, Electrical ignition sources in nuclear power plants: statistical, modelling and experimental studies, *Nucl. Eng. Des.* 213 (2–3) (2002) 209–221.
- [7] S. Lin, X. Huang, J. Urban, S. McAllister, C. Fernandez-Pello, Piloted ignition of cylindrical wildland fuels under irradiation, *Front. Mech. Eng.* 5 (2019) 54.

- [8] S. Hostikka, A. Matala, Modelling the fire behaviour of electrical cables, in: 20th International Conference on Structural Mechanics in Reactor Technology (SMiRT 20)–11th International Post Conference Seminar on Fire Safety in Nuclear Power Plants and Installations, 2009.
- [9] A. Matala, S. Hostikka, Pyrolysis modelling of PVC cable materials, *Fire Saf. Sci.* 10 (2011) 917–930.
- [10] A. Matala, Methods and Applications of Pyrolysis Modelling for Polymeric Materials, in: VTT Science, vol. 44, VTT Technical Research Centre of Finland Ltd., 2013, Dissertation.
- [11] T. Hehnen, L. Arnold, S. La Mendola, Numerical fire spread simulation based on material pyrolysis—An application to the CHRISTIFIRE phase 1 horizontal cable tray tests, *Fire* 3 (3) (2020) 33.
- [12] M.G.H. Fard, S. Hostikka, Combustion characteristics of non-charring polymer cylinders-experimental and numerical study, *Combust. Flame* 249 (2023) 112587.
- [13] W.L. Fons, Heating and ignition of small wood cylinders, *Ind. Eng. Chem.* 42 (10) (1950) 2130–2133.
- [14] S. McAllister, M. Finney, Autoignition of wood under combined convective and radiative heating, *Proc. Combust. Inst.* 36 (2) (2017) 3073–3080.
- [15] J. Mangs, A New Apparatus for Flame Spread Experiments, Tech. rep., 2008, VTT Working Papers 112. VTT, Espoo, 2009, 51 p.+ App.
- [16] J. Mangs, S. Hostikka, Vertical flame spread on charring materials at different ambient temperatures, *Fire Mater.* 37 (3) (2013) 230–245.
- [17] J. Mangs, S. Hostikka, Experiments and numerical simulations of vertical flame spread on charring materials at different ambient temperatures, *Fire Saf. Sci.* 10 (2011) 499–512.
- [18] K. Li, S. Hostikka, Embedded flame heat flux method for simulation of quasi-steady state vertical flame spread, *Fire Saf. J.* 104 (2019) 117–129.
- [19] K. McGrattan, S. Hostikka, R. McDermott, J. Floyd, C. Weinschenk, K. Overholt, Fire dynamics simulator user's guide, NIST Special Publ. 1019 (6) (2013) 1–339.
- [20] K.B. McGrattan, H.R. Baum, R.G. Rehm, A. Hamins, G.P. Forney, J.E. Floyd, S. Hostikka, K. Prasad, Fire Dynamics Simulator—Technical Reference Guide, National Institute of Standards and Technology, Building and Fire Research Laboratory, 2000.
- [21] C. Di Blasi, Modeling chemical and physical processes of wood and biomass pyrolysis, *Progr. Energy Combust. Sci.* 34 (1) (2008) 47–90.
- [22] K. Luostarinen, E. Verkasalo, Birch as Sawn Timber and in Mechanical Further Processing in Finland. A Literature Study, FI, 2000.
- [23] A.G. Bradbury, Y. Sakai, F. Shafizadeh, A kinetic model for pyrolysis of cellulose, *J. Appl. Polym. Sci.* 23 (11) (1979) 3271–3280.
- [24] C. Di Blasi, Physico-chemical processes occurring inside a degrading two-dimensional anisotropic porous medium, *Int. J. Heat Mass Transfer* 41 (24) (1998) 4139–4150.
- [25] C. Koufopoulos, A. Lucchesi, G. Maschio, Kinetic modelling of the pyrolysis of biomass and biomass components, *Can. J. Chem. Eng.* 67 (1) (1989) 75–84.
- [26] M.G. Grønli, G. Várhegyi, C. Di Blasi, Thermogravimetric analysis and devolatilization kinetics of wood, *Ind. Eng. Chem. Res.* 41 (17) (2002) 4201–4208.
- [27] M.J.J. Antal, G. Várhegyi, Cellulose pyrolysis kinetics: the current state of knowledge, *Ind. Eng. Chem. Res.* 34 (3) (1995) 703–717.
- [28] Y. Ding, C. Wang, S. Lu, Modeling the pyrolysis of wet wood using FireFOAM, *Energy Convers. Manag.* 98 (2015) 500–506.
- [29] S. Hostikka, A. Matala, Pyrolysis model for predicting the heat release rate of birch wood, *Combust. Sci. Technol.* 189 (8) (2017) 1373–1393.
- [30] H. Liu, C. Wang, A. Zhang, Numerical simulation of the wood pyrolysis with homogenous/heterogeneous moisture using FireFOAM, *Energy* 201 (2020) 117624.
- [31] D. Shen, M. Fang, Z. Luo, K. Cen, Modeling pyrolysis of wet wood under external heat flux, *Fire Saf. J.* 42 (3) (2007) 210–217.
- [32] M. Chaos, Spectral aspects of bench-scale flammability testing: application to hardwood pyrolysis, *Fire Saf. Sci.* 11 (1014) (2014) 165–178.
- [33] A. Matala, S. Hostikka, J. Mangs, Estimation of pyrolysis model parameters for solid materials using thermogravimetric data, *Fire Saf. Sci.* 9 (2008) 1213–1223.
- [34] X. Wang, C.M. Fleischmann, M.J. Spearpoint, Parameterising study of tunnel experiment materials for application to the Fire Dynamics Simulator pyrolysis model, *J. Fire Sci.* 34 (6) (2016) 490–514.
- [35] A. Rinta-Paavola, S. Hostikka, A model for the pyrolysis of two Nordic structural timbers, *Fire Mater.* 46 (1) (2022) 55–68.
- [36] T.L. Bergman, Fundamentals of Heat and Mass Transfer, John Wiley & Sons, 2011.
- [37] S.J. Ritchie, K.D. Steckler, A. Hamins, T.G. Cleary, J.C. Yang, T. Kashiwagi, The effect of sample size on the heat release rate of charring materials, *Fire Saf. Sci.* 5 (5) (1997) 177–188.
- [38] B.F. Magnussen, B.H. Hjertager, On mathematical modeling of turbulent combustion with special emphasis on soot formation and combustion, in: Symposium (International) on Combustion, Vol. 16, (1) Elsevier, 1977, pp. 719–729.
- [39] J.W. Deardorff, Stratocumulus-capped mixed layers derived from a three-dimensional model, *Bound.-Layer Meteorol.* 18 (1980) 495–527.
- [40] F. Nicoud, F. Ducros, Subgrid-scale stress modelling based on the square of the velocity gradient tensor, *Flow, Turbul. Combust.* 62 (3) (1999) 183–200.